Seismic Assessment of Small Modular Reactors: NuScale Case Study for the 8.8 Mw Earthquake in Chile

George Markou[1] and Filippo Genco[2]

[1] Department of Civil Engineering, University of Pretoria, Pretoria, South Africa
Email: george.markou@up.ac.za

[2] Universidad Adolfo Ibáñez, Santiago, Chile
Email: filippo.genco@uai.cl

Abstract

Reducing greenhouse gas emissions and improving energy production sustainability is a paramount of Chile's 2050 energy policy. This though, is difficult to achieve without some degree of nuclear power involvement, given that the geography of the country consists of many areas that are practically off-grid, whereas cannot be developed and financially exploited due to the lack of basic commodities such as water and electricity. Recently small modular reactors (SMRs) have gained lots of attention by both researchers and world policy makers for their promised capabilities of enhanced safety systems, affordable costs and competitive scalability. SMRs can be located in remote areas and at this time are being actively developed in Argentina, USA, Brazil, Russia, China, South Korea, Japan, India and South Africa.

Chile's 2010 earthquake and Fukushima's 2011 nuclear disaster have increased significantly both the population's fear and opposition to Nuclear Power Energy for the possible consequences of radiation on the lives of people. This paper aims to study the seismic resistance of a typical nuclear structure, being at time proposed in Small Modular Reactors, by using earthquake conditions typically seen in Chile. Since many designs are under study, a NuScale reactor from USA is analyzed under these extreme loading conditions. The major advantages of the NuScale reactor are in the power scalability (it can go from 1 to 12 reactor cores producing from 60 to 720 MWe), limited nuclear fuel concentration, modules allocated below grade and high strength steel containments fully immersed in water. The cooling effect beyond Design Basis Accident is ensured indefinitely, which induces a significant safety factor in the case of an accident.

For the purpose of this study a detailed 3D detailed structural model was developed, reproducing the NuScale reactor's reinforced concrete framing system, where nonlinear analyses was performed to assess the overall mechanical response of the structure. The framing system has been tested under high seismic excitations typically seen in Chile (Mw > 8.0), showing high resistance and capability to cope with the developed forces due to its design. Based on a Soil-Structure Interaction analysis, it was also found that the NuScale framing system manages to maintain a low-stress level at the interaction surface between the foundation and the soil, where the structural system was found to be able to withstand significant earthquake loads. Finally, further investigation is deemed necessary in order to study the potential damages of the structure in the case of other hazards such as tsunami events, blast loads, etc.

***Keywords**: Small Modular Reactors, Chile 2050 Energy Policy, 3D Detailed Finite Element Modeling, Seismic Resistance, Soil-Structure Interaction, Reinforced Concrete*

1. Introduction

The effect of the 27th of February 2010 earthquake in Chile and the events of 11th of March 2011 earthquake in Fukushima, Japan, have shown that nuclear power plants can be subjected to extreme events eventually leading to a nuclear disaster and might not be ideal for a country that is seismically active and at high risk such as Chile. Many studies have been performed since then, that have proved that March 11th earthquake in Japan had insignificant seismic effects despite the high magnitude recorded (M_w=9.0) on the nuclear reactor structures [1]. The effects of the waves of the subsequent tsunami were much higher than the historical record up to that point, leading to a full flooding of the inner plain as well as of the power plant [2]. This sequence of events initiated the Fukushima-Daiichi disaster with eventual core meltdown of the three cores due to insufficient cooling provided before the water flood by the emergency Diesel generators.

Fukushima's disaster outcomes have led to intensive research and engineering efforts to include beyond design-basis accidents not considered in original constructions or projects [3-7]. Several key issues have been also identified in both the actual safety culture in the nuclear industry [8-10] and limitations to the actual severe accidents management strategies [11-13].

Next generation nuclear power reactors have been developed worldwide under the direction of the International Atomic Energy Agency (IAEA) in the last 20 years. "Small" reactors produce less than 300 MWe while "medium" reactors have a typical maximum output capacity around 700 MWe [14]. There has been lots of interest in governmental agencies as well in the research community to develop these new concepts due to the many superior advantages promised with respect to the past [14-15]. Safety has been largely enhanced using new design concepts: inherent and passive safety systems, modularity for cheap massive factory-built production with high manufacturing quality, small size and transportability, power scalability and economic affordability [15]. Small nuclear Reactors (SMRs) under development have high flexibility and various sizes to satisfy the future energy demands.

There are essentially five major groups of small modular reactors (SMRs). Light water reactors (Pressurized water reactors -PWRs and Boiling water Reactors -BWRs) and heavy waters reactors (HWRs) use decades of industrial experience matured around the world in large scale nuclear power plants to provide a highly safe design with compact dimensions and costs. Gas cooled reactors (GCR) or fast breeders liquid metal cooled reactors (LMFBR) instead, have very advanced designs but are still in the research phase and lack the solid testing and decades of industrial experience so far acquired in the Nuclear Industry. For this reason, they are not considered in this study as an immediate possibility to be implemented in Chile.

Nuclear power generation provides a very promising alternative in the reduction of greenhouse gases (GHG) and potentially could become the cheapest source of energy to fulfill energy challenges across countries in South America [16]. Nuclear power development in Chile has been hindered mostly by political indecision and people's fear over nuclear power plants and their capacity to undertake extreme natural events [9, 17-18]. This can be mainly attributed to the lack of education in energy matters and the fear that resulted from the safety failures that have occurred when implementing current nuclear energy technology. For this reason, this study takes into consideration a newly introduced SMR design and examines the structural response this reactor would have in case of a large seismic event similar to those of 2010 in Chile and 2011 in Japan.

This paper is subdivided in 3 major parts. In the first part a brief summary of the characteristics of light water cooled SMR reactors potentially to be used in Chile, are reviewed. In the second part, the geometrical and mathematical models used herein for the finite element (FE) analyses are described. In the third part, the numerical results are presented and discussed at the light of available literature data. In addition, future research efforts and recommendations for the correct implementation of future policies and decisions are proposed.

2. Light Water Cooled SMRs solutions for Chile

Since Chile has not yet developed a full nuclear energy policy and presents also a high frequency of natural events, it is suggested the adoption of a small modular reactor with advanced certification program and testing already performed at this time. It is also advisable to choose a model that does not differ too much from the conventional nuclear engineering applications so that the past industrial know-how can be fully exploited. Three major reactor designs respond to these characteristics: 1) the CAREM-25 [14,19-20] being built at this time in Argentina and based on an advanced passive safety PWR concept; 2) the SMART, designed and built in South Korea and fully licensed by the Korean Nuclear Safety and Security Commission in 2012; SMART is also based on the PWR design [21-22] and 3) the NuScale, designed in USA and with enhanced safety features is based on natural circulation. NuScale has targeted 2023 as the possible year of commercial operations [23-24]. All these three reactors are water-cooled and present characteristics of modularity [14-15, 25] and innovative safety features, which grant much larger margins of safety when they undergo extreme natural events.

2.1. CAREM-25 Reactor (Argentina)

CAREM-25 is an Argentinian SMR developed staring from 1984. It can generate up to 100 MWth or 25 MWe. The goal of its design is to establish a highly economically competitive and safe reactor. All major primary components are allocated in the same compartment with the reactor core: the control rod driving mechanism, the once-through steam generators and natural circulation is used in the primary circuit of this integral PWR. CAREM-25 safety systems are fully passive and do not need any operator intervention to enter in function. All safety systems are duplicated: reactor protection system, shutdown systems, safety valves, low-pressure injection system and heat removal system. Natural circulation transfers core decay heat to a dedicated pool inside the containment and then to the suppression pool.

CAREM-25 has a predicted core damage frequency (per reactor year) of 10^{-6} and a grace period of station blackout of 72 hours. Currently, the CAREM-25 is under construction with the licensing approval obtained in 2010. It is also important to note at this point that, Argentina is not considered to be a seismically active country where large earthquake events have been recently recorded, thus acquiring the corresponding licensing approval for constructing the CAREM-25 here in Chile should foresee a more rigorous investigation especially when dealing with earthquake loads and the resistance of the proposed framing system during a tsunami event.

2.2. SMART SMR Reactor (South Korea)

SMART is a small integral PWR design proposed by KAERI in South Korea with a rated electric power of 100 MWe or 330 MWth. The SMART SMR reactor has been fully licensed in South Korea in 2012 by the Korean and Security commission and it has a predicted core damage frequency equal to 10^{-6} (per reactor year).

Inherent safety features and passive safety systems are all integrated in the SMART design configuration, aiming to achieve high safety standards with reduced costs and economy of scale. Simplification, modularization and reduction in construction times aim to achieve a high affordability of this reactor. Low power density ensures high margin of controllability during transients. All primary components as steam generators and core structures are contained inside the reactor pressure vessel.

The SMART engineered safety systems are designed to function automatically providing passive residual heat removal, shutdown and safety injection. The reactor is also designed against over-pressurization and by using integral arrangement only small-break Loss of Coolant Accidents (LOCA) are possible. Both active and passive systems are combined to achieve a high level of safety with safety features all fully validated by full-

scale or scaled tests. After Fukushima's events, fully passive safety systems have been developed and adopted in this case for eliminating the dependency on the Emergency Diesel Generator [14].

2.3. NUSCALE SMR Reactor (USA)

NuScale design proposes a reactor made up by a maximum of twelve independent reactor modules each producing a thermal power of 200 MWth and gross electric power around 60 MWe. Each reactor foresees a high-pressure containment vessel surrounded by a second steel vessel. All power modules are allocated and immersed in a common below-grade pool. Both primary system and containment are pre-fabricated and transported with the most economical means possible (train, truck or ship) to the plant's final site. This construction approach reduces the cost, while the on-site time for constructing the reactor is estimated to be about 36 months.

The NuScale reactor operates on natural convection instead of forced water circulation in case of power loss and adopts fully passive safety systems. The innovative design principles ensure high levels of safety providing in all possible scenarios, a stable and long term cooling of the core(s). Apart from the containment vessels, the emergency core cooling system and the passive decay heat removal system ensure severe accident mitigation.

The innovative feature of the sub-grade pool ensures continuous cooling for at least 30 days for all 12 modules, after which simple air-cooling is sufficient to remove the residual decay heat without core damage. The below grade pool design approach not only ensures enhanced cooling and safety features, but provides a further physical barrier to the accessibility of the fuel and an improved mechanism to dissipate energy in case of strong earthquakes. The reactor modules are very compact (24.6 m tall and 4.6 meter in diameter) and can be fully prefabricated in parallel off-site ensuring modularity, flexibility and scalability. Since each power module is built to operate independently, some modules can be dedicated to full electricity production and others can be used for providing a thermal source via steam extraction, augmenting the applications possible (i.e. desalination in addition to power production). NuScale provides very high levels of resilience to events similar to the one happened in Fukushima (Japan) in 2011 and of course possible to occur in Chile [26]. NuScale module containment can resist to pressure as high as twelve times the traditional containment due to its small diameter. The predicted core damage frequency (per reactor year) is calculated at 10^{-9}.

Each reactor module is self-contained with its own shutdown system independent from the others. An assembly, reassembly location inside the major building is to be used as inspection and refueling area without disruptions to the other core that keep operating. This ensures continuity in the electrical power production and reduced grid disruption.

The NuScale prototype is chosen for a more detailed earthquake resilience study [7] given that it has incorporated all suggestions and engineering modifications proposed in the after math of the Fukushima-Daiichi disaster [3]. This is achieved in terms of loss of heat sink, hydrogen detonation, enhanced capacity to contain radioactive releases due to the double vessel (containment and pressure) and the fact that there is no need for electrical emergency supply since each module can shut down safely with no human intervention. Moreover, no external additional water and no AC/DC power are required.

Furthermore, this type of reactor is chosen to be studied herein for the following major reasons: a) its footprint is small and it is highly scalable (power can go from 60 up to 720 MWe) b) in USA its certification process with NRC is currently in an advanced state c) studies related to its safety, show that in case of total power loss (as the one happened in Fukushima) there would be no dependence on external forced cooling (Diesel generators) whereas it would passively cooled via natural circulation. The power plant could independently keep this cooling regime for at least 30 days at full installed power [24] after which it could be cooled by air and without any cooling loss thereafter; d) the calculated core damage frequency is among the lowest of the

many designs under development or review in the world and far better than the other two prototypes (CAREM-25 and SMART) under investigation (10^{-9} versus 10^{-6}).

Its commercial deployment is predicted by 2023 in USA and would provide enough time for the Chilean authorities to put into operation a legal framework able to fully embrace safe nuclear power, therefore, e) it would eliminate any dependence from neighboring states (i.e. Argentina and its technology) since neighboring countries cannot be a fully reliable partner for Chile for energy source acquisition [27]. NRC's approval of the complete design of the NuScale reactor is expected by 2020, with the 1st module to be delivered in Idaho in 2023 and the 12th in 2024.

3. Numerical Modeling of NUSCALE SMR Structures

For the needs of this research work, FE analyses were performed to investigate the structural response of the NuScale reactor building [14] reproduced schematically in Fig. 1 and its ability to undergo extreme earthquake excitations. SAP2000 [28] and Reconan FEA [29] were used for constructing the meshes used herein for determining the overall seismic response of the building. The soil-structure interaction (SSI) phenomenon is also taken into account in order to study the developed stresses at the concrete frame and the soil domain due to various load types that are applied on the structure.

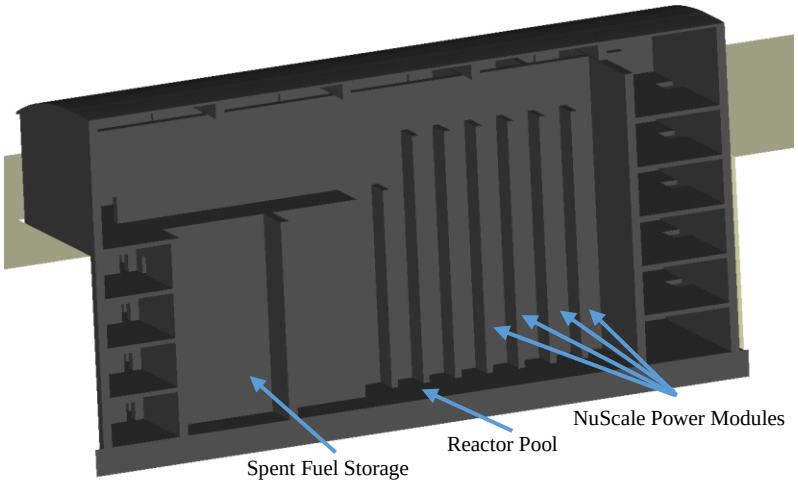

Figure 1 Schematics of NuScale reactor plant as in [14]

3.1. Geometry and Reinforcement Details

The numerical assessment of the framing system performed in this research work foresaw the study of the reactor building (RB), which was designed based on the Eurocode 2 provisions [30]. The geometry of the framing system was based on the geometrical features depicted in Figs. 1-3 given that a detailed drawing of the frame was not available. Dimensions have been evaluated using data provided in the literature [14, 23-24, 26]. A typical plan view of the structure can be seen in Fig. 2, where the 3 m thick raft slab and the 4th basement plan view are shown (Level -4). It must be noted here that, the NuScale design has galleries on both sides, which were not included in this study for simplicity reasons. The total length of the building is 75.25 m, with a 30 m width, while the total height of the structure from the foundation's base is 39.55 m (out of which 25 m are underground; see Fig. 3). As it is shown in Fig. 3, the raft slab has a 1 m foot extending around the 1 m thick retaining walls. Furthermore, the design foresees that the 5 levels have a height of 5.5 m (from slab to slab) as shown in sections *a-a* and *b-b*, where the last level has a maximum height of 9.55 m. The thickness of the internal walls varies between 0.75 and 1 m, where all slabs have a thickness of 50 cm. Finally, the roofing system foresees a slab thickness of 30 cm and four arch beams that have a rectangular section of 100x205 cm.

Table 1 contains the information related to the assumed reinforcement used to develop the 3D detailed model that was used to check for crack openings due to operational loads, including the soil lateral pressure. Based on the reinforcement details provided in Table 1, the structure was reinforced with 40 mm in diameter rebars at the raft slab, where the exterior and interior walls use 25 mm longitudinal rebars and 20 mm shear reinforcement. The roof slab is reinforced with 14 mm rebars with a spacing of 100 mm in both directions (top and bottom) and the slabs were reinforced with 20 mm in rebars at the top and bottom along the x and y directions. The use of a unified reinforcement detailing in both slabs and shear walls was chosen for practical reasons in an attempt to assure a proper model development that will be error free. As it is going to be presented in the next sections, the 3D detailed approach foresees the use of embedded rod FEs for discretizing the steel reinforcement in an exact geometrical manner. Therefore, the construction of the embedded rebar mesh becomes less cumbersome and more time efficient. Fig. 4 shows the embedded rebar mesh that was constructed based on the reinforcement detailing provided in Table 1. As it can be observed, the beams are reinforced with 40 mm longitudinal rebars and 30 mm rebars along the web of the RC section, where 16 mm in diameter shear reinforcement is foreseen.

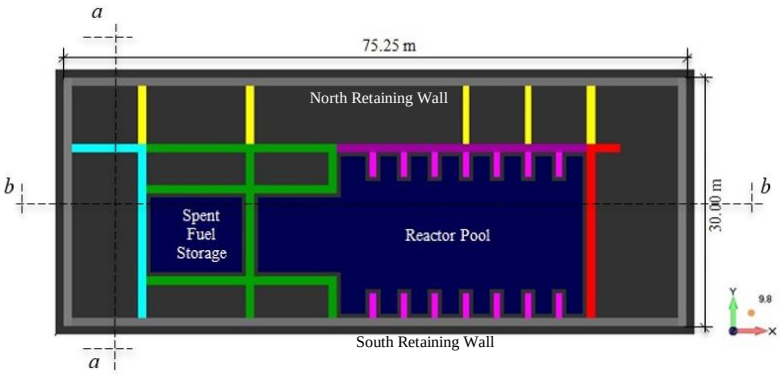

Figure 2 Reactor Building Plan View of level -4.

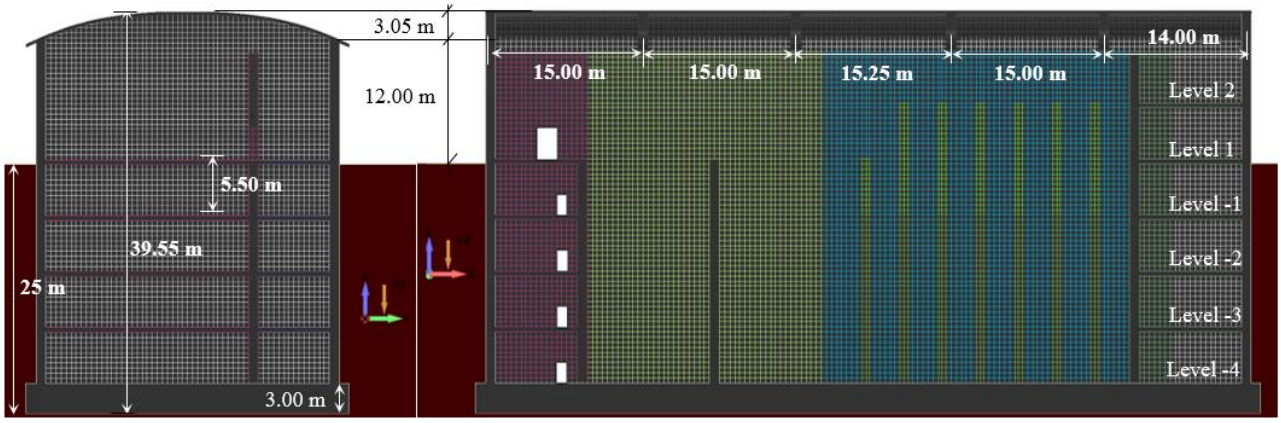

Figure 3 Reactor Building Sections (Left) *a-a* and (Right) *b-b*.

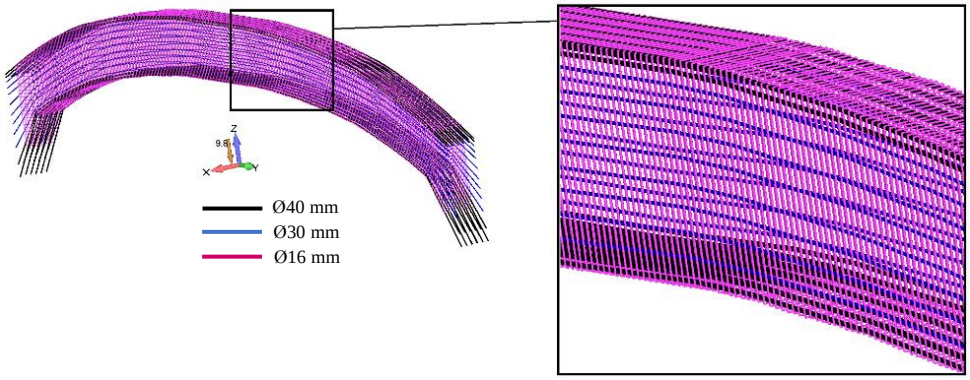

Figure 4 Reactor Building. 3D RC arch beam reinforcement. Finite element mesh.

Table 1 Reinforcement Table

a/a	Description	Direction	Diameter (mm)	Num. of Layers	Spacing (mm)	Section Area (cm^2/m)*	Reinf. ratio ρ	
1	Foundation (Raft Slab)	X	40	4	100	30,000	1.68%	
		Y	40	4	100	30,000	1.68%	
		Edge Vertical	30	2	100	-	-	
		Edge Horizontal	25	1	200	-	-	
2	Exterior Wall	Vertical	25	4	100	10,000	1.96%	
		Horizontal	20	2	100	10,000	0.63%	
3	Slabs	X	20	2	100	5,000	1.26%	
		Y	20	2	100	5,000	1.26%	
4	Shear Walls	Vertical	25	2	100	10,000 and 7,500	0.98%	
		Horizontal	20	2	100	10,000 and 7,500	0.63%	
5	Walls Next to Reactors	Vertical	25	2	100	7,500	1.31%	
		Horizontal	20	2	100	7,500	0.84%	
6	Roof	X	14	2	100	3,000	1.03%	
		Y	14	2	100	3,000	1.03%	
7	Beams	Longitudinal	40	2 top + 2 bottom	12 bars top + 12 bars bottom	20,500	1.51%	2.08%
		Torsion	30	1 left + 1 right	8 bars left + 8 bars right	20,500	0.57%	
		Stirrups	16	6 legs	100	-	1.21%	

*Applicable for surface structural members. For the case of beams the section area unit is in cm^2.

3.2. Material Models

Linear and nonlinear analyses were performed for the numerical investigation of the RB through the use of SAP2000 and Reconan FEA. Given the limited capabilities of SAP2000 in performing 3D detailed nonlinear analysis, the software was used to perform modal and linear analyses of the framing system, without considering the soil domain. In addition, a single arch beam was analyzed through SAP2000 for estimating the capacity of the beam under vertical nonlinear loading conditions. The concrete was assumed to have an ultimate compressive strength f_c of 50 MPa (cylindrical strength, which was assumed for all performed analysis in this work), whereas a plastic hinge (see data in Fig. 5) was assigned at the ends and midspan of each frame object in order to capture the nonlinearities at the section level.

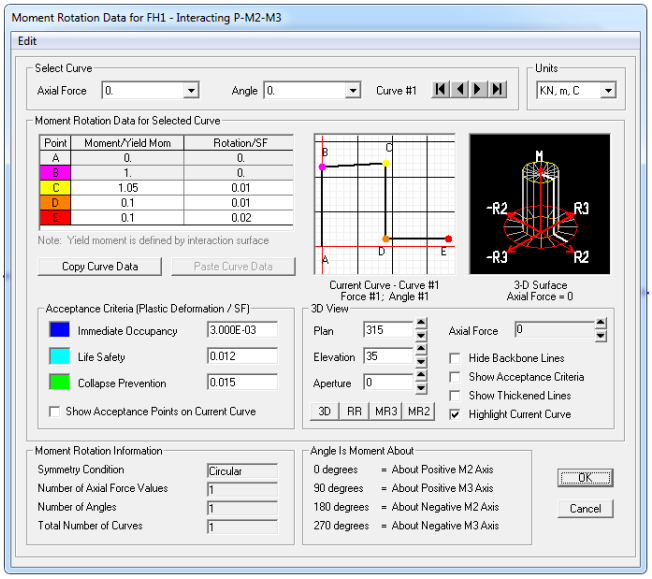

Figure 5 Plastic hinge data, used for the SAP2000 arch beam model.

As it was described in [31], when using the 3D detailed modelling approach, the concrete is discretized with hexahedral elements that treat cracking with the smeared crack approach and the reinforcement is modeled with the embedded rod element [32]. The constitutive material model of concrete, is based on the proposed algorithm presented in [33], where the mechanical behavior of RC members can be assessed under monotonic and cyclic loading conditions. The adopted model is also integrated with a flexible crack closure criterion, which induces numerical stability during the cyclic analysis as it was described in [34]. Even though the simulations performed in this research work foresaw only nonlinear monotonic loading, the opening and closing of cracks can occur at any loading step due to internal stress redistribution, thus the numerical ability to account for this phenomenon is provided through the adopted 3D concrete material model. For the modeling of cracks, the smeared crack approach is implemented herein, an approach that was presented by Rashid [35] as a continuation of the method proposed by Gonzalez-Vidosa et al. [36]. The smeared crack model numerically accounts for crack openings by modifying the material constitutive matrix, which is used to compute the stiffness matrix and stresses at the corresponding integration point (Fig. 6).

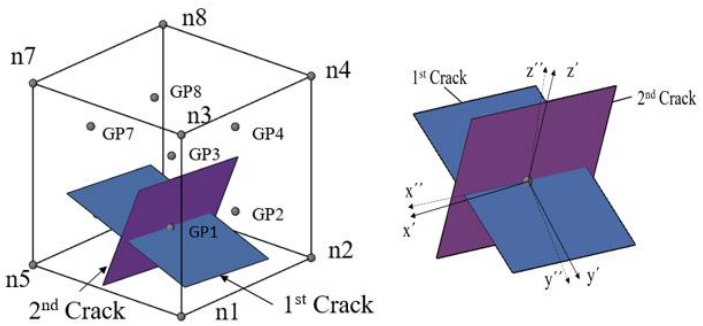

Figure 6 Local axes for the case of two cracks at a specific Gauss point. [33]

The crack opening strategy during each load increment foresees the use of the unified total crack approach (UTCA) [37], which foresees that crack openings and closures are to be treated in a unified way within every Newton-Raphson internal iteration. In the case where a Gauss point cracks the concrete material assumes that it loses all of its carrying capacity along the vertical direction of the crack. The strength envelope of concrete through which the algorithm determines whether a Gauss point is cracked is provided in Eq. 1 and it's based on the Willam and Warkne (1974) formulae.

$$\tau_{0u} = \frac{2\tau_{0c}(\tau_{0c}^2 - \tau_{0e}^2)\cos\theta + \tau_{0c}(2\tau_{0e} - \tau_{0c})\sqrt{4(\tau_{0c}^2 - \tau_{0e}^2)\cos^2\theta + 5\tau_{0e}^2 - 4\tau_{0c}^2\tau_{0e}^2}}{4(\tau_{0c}^2 - \tau_{0e}^2)\cos^2\theta + (2\tau_{0e} - \tau_{0c})^2} \quad (1)$$

where the rotational variable θ defines the deviatoric stress orientation on the octahedral plane. The τ_{0e} (θ=0°) and τ_{0c} (θ=60°) are corresponded to the state of $\sigma_1=\sigma_2>\sigma_3$ (triaxial extension) and $\sigma_1>\sigma_2=\sigma_3$ (triaxial compression), respectively and expressed analytically by experimental data.

As it was presented in [34], the material modeling procedure also uses a flexible crack closing criterion that was found to play a significant role during the opening and closing of cracks, thus achieving a faster convergence ratio. According to the proposed criterion in [34], the closure of cracks is expressed based on the following equation:

$$\varepsilon_i \le \left(b - \frac{n_{cr} - 1}{n_{tot}} \right) \varepsilon_{cr} \quad (2)$$

where ε_i is the current strain in the i-direction that is normal to the crack plane and ε_{cr} is the strain that causes cracking formation. Parameter b is the number of the imposed displacement branch of the load history, while n_{cr} and n_{tot} are the numbers of increment that the crack is formed at and the total number of increments that an imposed displacement branch is divided into, respectively. More details on the cracks closure criterion can be found in Mourlas et al. [34].

For the modeling of the steel reinforcement (embedded rebar elements found within the hexahedral mesh), the algorithmic framework adopts the use of the Menegotto-Pinto [38] model that takes into account the Bauschinger effect (see Fig. 7). The stress-strain relation in this case takes the following form:

$$\sigma^* = b\varepsilon^* + \frac{(1-b)\varepsilon^*}{(1+\varepsilon^{*R})^{1/R}} \quad (3)$$

where,

$$\varepsilon^* = (\varepsilon - \varepsilon_r)/(\varepsilon_0 - \varepsilon_r), \quad (4)$$

$$\sigma^* = (\sigma - \sigma_r)/(\sigma_0 - \sigma_r) \quad (5)$$

$$R = R_0 - a_1\xi/(\alpha_2 + \xi) \quad (6)$$

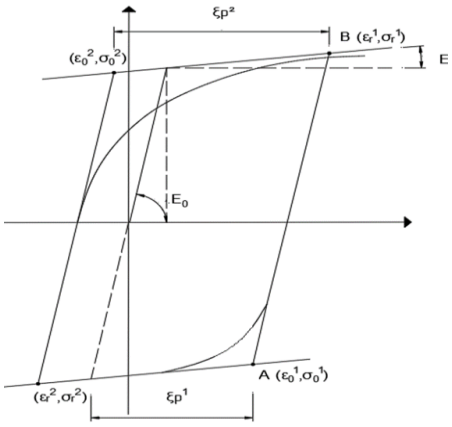

Figure 7 Menegotto – Pinto steel model. [33]

A full bond is assumed between the rebars and the concrete material [31], where for all analyses performed in this research work, the steel Young modulus of elasticity and the yielding stress were equal to 190 GPa and 500 MPa, respectively. It must be noted at this point that the von Mises material yielding criterion was also used for modeling the mechanical behavior of the soil domain as described in [39], whereas this material

model is also used for the case where the RB's model takes into account the SSI phenomenon. Therefore, when the model uses hexahedral elements for discretizing the soil domain, the RC framing system of the RB is modeled by using the von Mises yielding criterion so as to account for material nonlinearities.

3.3. Mesh Construction

Two 3D detailed models, Model A and B, were developed through the use of Femap and analyzed with Reconan FEA for the needs of this study. The first model foresaw the discretization of the RC building with the 3D detailed approach and foresaw the application of fixed supports at the base of the raft foundation, while the lateral soil pressure was applied at the retaining walls as forces (Model A). A detailed discretization of the framing system was performed through the use of the isoparametric 8-noded hexahedral FE, as illustrated in Fig. 8, based on the geometry shown in Figs. 2 and 3. The hexahedral mesh size that was used to discretize the concrete domain was 0.5 m, while for the case of shear walls that had a thickness of 0.75 m, the hexahedral size was set to 0.375 m. As it can be observed from Fig. 8, the raft slab was divided into 3 layers, each of 1 m thick, in an attempt to maintain the number of hexahedral elements relatively low without losing the required numerical accuracy. A mesh sensitivity analysis was performed by using an initial discretization of 1 m hexahedral elements (see Fig 9), and it was found that the finer discretization derived deformations that were close to the ones computed by the mesh presented in Fig. 8. Therefore, the final mesh depicted in Fig. 8 was the one used for the numerical assessment of the RB in this study.

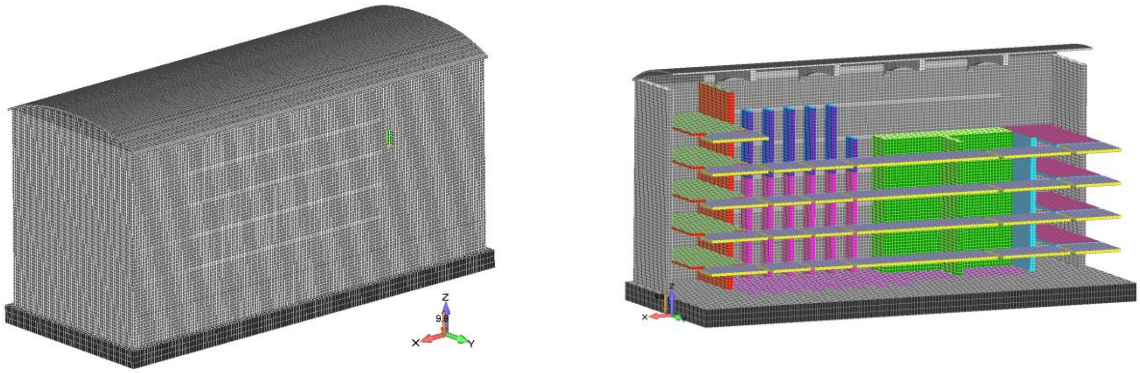

Figure 8 Reactor Building Model A. Hexahedral finite element mesh of the RC framing system (Left) Full model and (Right) View of the South exterior wall, reactors walls, slabs and half of the roofing system.

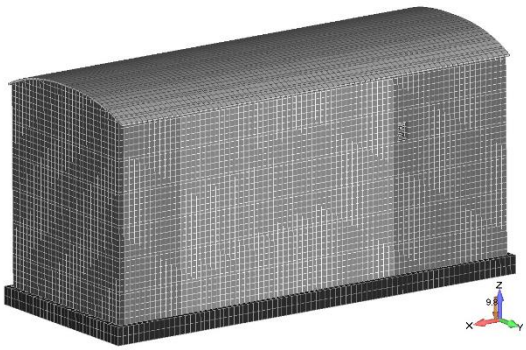

Figure 9 Reactor Building Model A. Coarser hexahedral finite element mesh of the RC framing system.

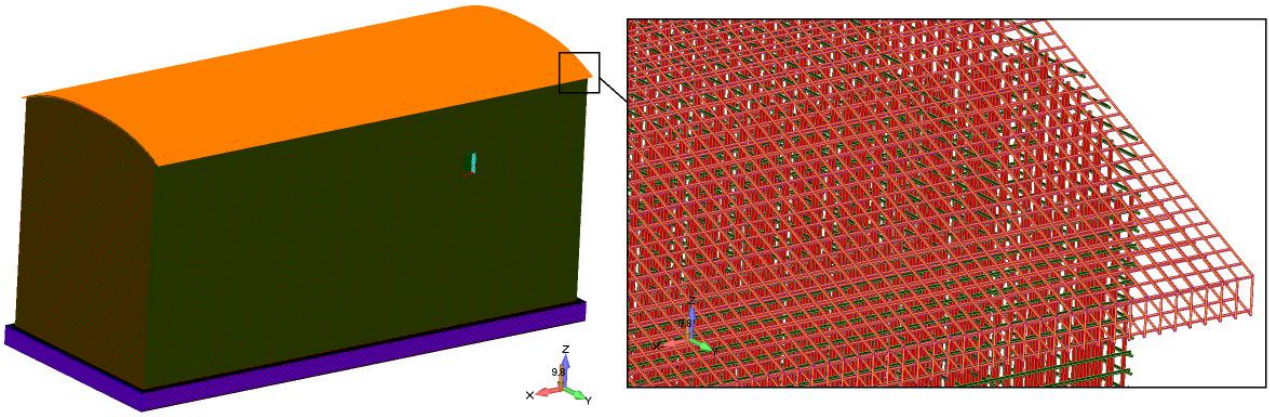

Figure 10 Reactor Building Model A. Embedded rod element finite element mesh.

Model A, which foresaw the discretization of the reinforcement through the rod FE, was used to investigate the underground framing system of the structure and the case of potential crack openings due to the lateral soil pressure when the plant undertakes operational loads. According to Table 2, a total of 172,112 hexahedral elements were used so as to discretize the RB's framing system, where 2,530,843 embedded rebar elements were used to model the reinforcement found within the concrete domain. Fig. 10 shows the FE mesh of the embedded rebars that were constructed for the needs of Model A, while in Fig. 4 the corresponding embedded rebar mesh that was developed for one of the four arch beams can be seen. It must be noted here that, the assumed boundary conditions of Model A foresaw fixing the nodes found at the base of the raft slab.

Table 2 Finite element mesh with and without soil.

Model	Hexahedral Elements	Hexahedral Nodes	Embedded Rebars	Spring Elements	Dofs	Stiffness Matrix (Gb)
Model A	172,112	261,856	2,530,843	-	754,563	34
Model B	316,962	429,244	-	18,662	1,204,260	74

Model B, was constructed in order to study the structure's behavior under static and earthquake loads when accounting for the SSI phenomenon. The complete hexahedral mesh can be seen in Fig. 11, which foresees the use of 160,536 concrete hexahedral elements and 156,426 soil hexahedral elements. In order to take into account a more realistic interaction between the soil and concrete domains, spring elements were used to decouple the nodes at the interface of the retaining walls and the soil domain. The springs used herein, were integrated with a material that can resist only to compressive forces thus when it is under tension, the spring's resistance is automatically set to zero. In addition to that, the friction forces at the interface are also set to zero so as to derive a maximum SSI effect that will result to a more flexible overall numerical behavior of the structure. In regards to the boundary conditions that were applied on Model B, they foresaw the fixation of all the nodes found at the base of the soil domain, where the nodes located on the boundaries perimetrically of the soil domain were restraint along the x and y global directions. This is a typical approach so as to allow the simulation of settlement but at the same time avoid any lateral expansion of the soil domain.

In order to highlight the level of accuracy and corresponding computational demand of the developed models in this study, which are (to the best of the authors' knowledge) currently the most detailed models constructed to study the mechanical behavior of a NuScale RB (see Model A) with SSI considerations (see Model B), the work of Sextos et al. [46] is cited herein for comparative purposes. In their work, the dynamic behavior of a containment building was studied for uplift phenomena, by accounting the SSI effect through a modeling approach similar to the one presented in Fig. 11. In order to discretize the 85.8m tall Nuclear Power Plan containment building [46], hexahedral FEs were used for the shallow raft slab foundation that was connected to the soil hexahedral mesh, while the shell FE was adopted for discretizing the cylindrical shaped walls of the structure (the diameter of the building was 43m). The shell FEs had a size of approximately 5x5x1.5m, which

constitutes a very coarse mesh due to the computational demand of the derived model [46]. In our research work, presented in this section (see Figs. 9 and 11), the RC volume of 5x5x1.5m is discretized with 300 hexahedral FEs. This is also the main reason why dynamic analyses were not performed in this study, which is a subject of future research.

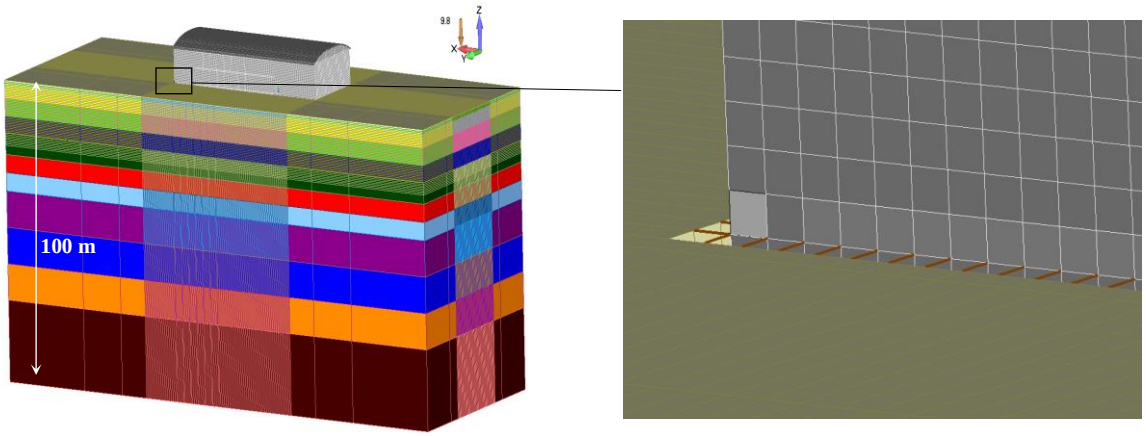

Figure 11 Reactor Building Model A. Final hexahedral finite element mesh of the (Left) RC framing system with soil and (Right) Spring elements at the concrete-soil interface.

Fig. 11 shows the soil domain mesh that foresaw the use of 12 layers with thicknesses and material properties found in Table 3. As it was stated above, the RB structure reaches a maximum underground depth of -25 m, therefore, the soil domain that was modeled had a total depth of 100 m and its length and width were set to 123.25 m and 84 m, respectively. The corresponding material parameters for each layer where computed based on the Ground Types A and B of Eurocode 8 (Table 3). The Shear wave velocities and unit weights were assumed to represent a random but realistic soil profile, whereas the young modulus of elasticity was calculated according to Eq. 7.

$$E = 2(1+\mu){v_s}^2\rho \tag{7}$$

As shown in Table 3, the minimum shear wave velocity was set to 215 m/s for the top soil layers (up to 6 m depth), while the deeper the soil layer is, the higher the shear wave velocity gets. In general, characteristics of soil materials are site-specific thus should derive from a relative geotechnical report based on the selected construction site in Chile. It must be also noted at this point that, the stability slope is not a key design parameter herein given that the plant layout assumes a uniform and graded site.

In regards to the loads that were accounted for, the self-weight of all structural members was computed automatically by using a 25 kN/m^3 nominal weight for the case of the RC material, while a 7 kN/m^2 was applied as a live load on all slabs except the roof where a 0.3 kN/m^2 was assumed. At the area of the reactor pool and the spent fuel storage, the hydrostatic pressure was applied for the scenario where they are both considered to be full (operating scenario). The static load due to the 12 Nuclear Reactor Modules (NRM) was accounted for, where each NRM was assumed to have an approximate weight of 9,600 kN that was applied at the connection points with the reactor shear walls, while the load due to the bioshields was set to 900 kN. These loads were applied directly on the nodes of the reactor walls at the connection areas (at the middle of each wall). In addition to that, an extra load of 10,000 kN was applied at the slab where the NRM maintenance area is located at, while the static load due to the crane was also accounted for. Loads that relate to distributed systems such as cables, piping, etc. were neglected given that their weight was assumed that it will not have a significant effect on the overall structural response (< 1% of the mass of the supporting system). The seismic load that was applied on the SSI model will be discussed in Section 3.7.

In addition to the two detailed models developed for the modeling requirements of this study, a third model was developed through the use of SAP2000 that foresaw the discretization of the framing system with shells and frame FEs (see Fig. 12). The material properties that were defined within the SAP2000 model were the same as described above (C50 concrete; E_c = 30 GPa, f_c = 50 MPa and ν = 0.2) and the geometry of the model was constructed based on Figs. 2 & 3 in achieving identical mesh geometries that were used for validation and comparative purposes. It must be noted at this point that, the SAP2000 model was used to compute the modes of the under study RB, where elastic analysis was also performed for the operational and lateral soil loads.

Table 3 Soil layers. Geometric and material properties.

Layer No.	Thickness (m)	Depth (m)	Shear Wave Velocity v_s (m/s)	Unit Weight γ (kN/m^3)	Poisson's Ratio ν	Young Modulus E (MPa)	Compressive Strength $f_{c,soil}$ (kPa)
1	0.50	-0.50	215.00	18.5	0.35	235.366	1000.0
2	1.00	-1.50	215.00	18.5	0.35	235.366	1000.0
3	4.50	-6.00	215.00	18.5	0.35	235.366	1000.0
4	6.00	-12.00	300.00	18.5	0.35	458.257	1200.0
5	6.00	-18.00	355.00	18.5	0.35	641.687	1400.0
6	6.50	-24.50	365.00	18.5	0.35	678.347	1500.0
7	6.00	-30.50	345.00	18.5	0.35	606.045	1500.0
8	6.00	-36.50	350.00	18.5	0.35	623.739	1550.0
9	12.00	-48.50	355.00	21.0	0.35	728.401	1600.0
10	12.00	-60.50	360.00	21.0	0.35	749.064	1700.0
11	12.00	-72.50	365.00	21.0	0.35	770.016	1800.0
12	27.50	-100.00	2440.00	23.5	0.25	35654.842	25000.0

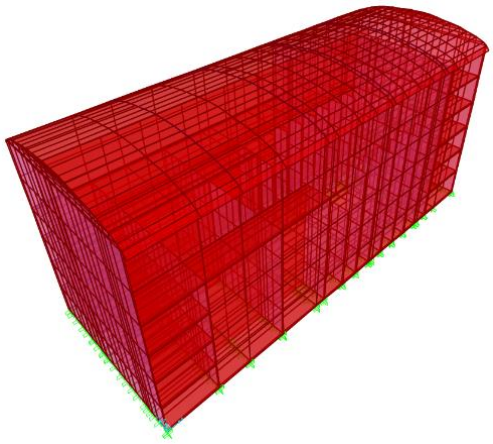

Figure 12 Area objects that were used to generate the finite element mesh of the SAP2000 model.

3.4. Modal and Preliminary Analyses

The framing system of the RB is basically a box-like structure with long shear walls that add significant stiffness to the overall mechanical behavior of the structure. In order to investigate the mechanical behavior of the structural system, a modal analysis was performed through the use of SAP2000, where the first 120 modes were computed. Fig. 13 shows the first 12 fundamental modes, whiles modes 15, 20, 30, 40, 50, 60, 70, 80, 90, 100, 110 and 120 can be depicted in Fig. 14. According to the modal analysis, the long structural RC walls and the roofing system controlled the deform shapes of the first modes, whereas the roof and slabs were found to result a more flexible behavior in comparison to the stiffer internal and exterior shear walls. Furthermore,

fundamental mode 6 derived a period of T_6 = 0.1406 s and was found to be the largest period of the structure that included a translational oscillation of the framing system along the y-axis (parallel to the short side of the RB). This mode, which is expected to be activated during a seismic event thus generate inertia forces along the short dimension of the structure, was also used to compute the seismic loads along the global y-axis of the RB; the direction that is considered to be the most vulnerable in terms of developing the largest horizontal deformations during a seismic excitation.

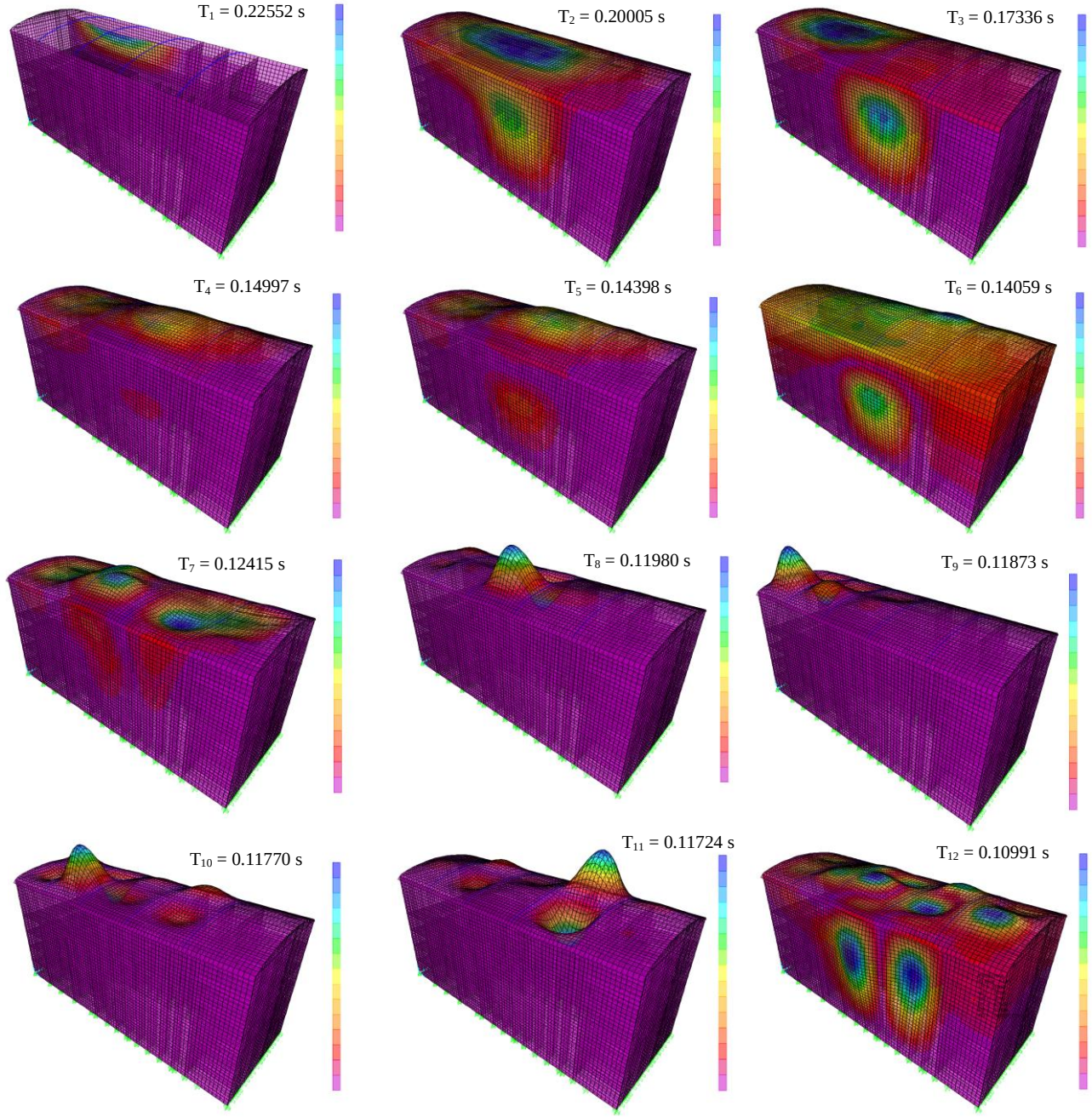

Figure 13 Modal shapes 1-12 of the Reactor Building. SAP2000 displacement contours.

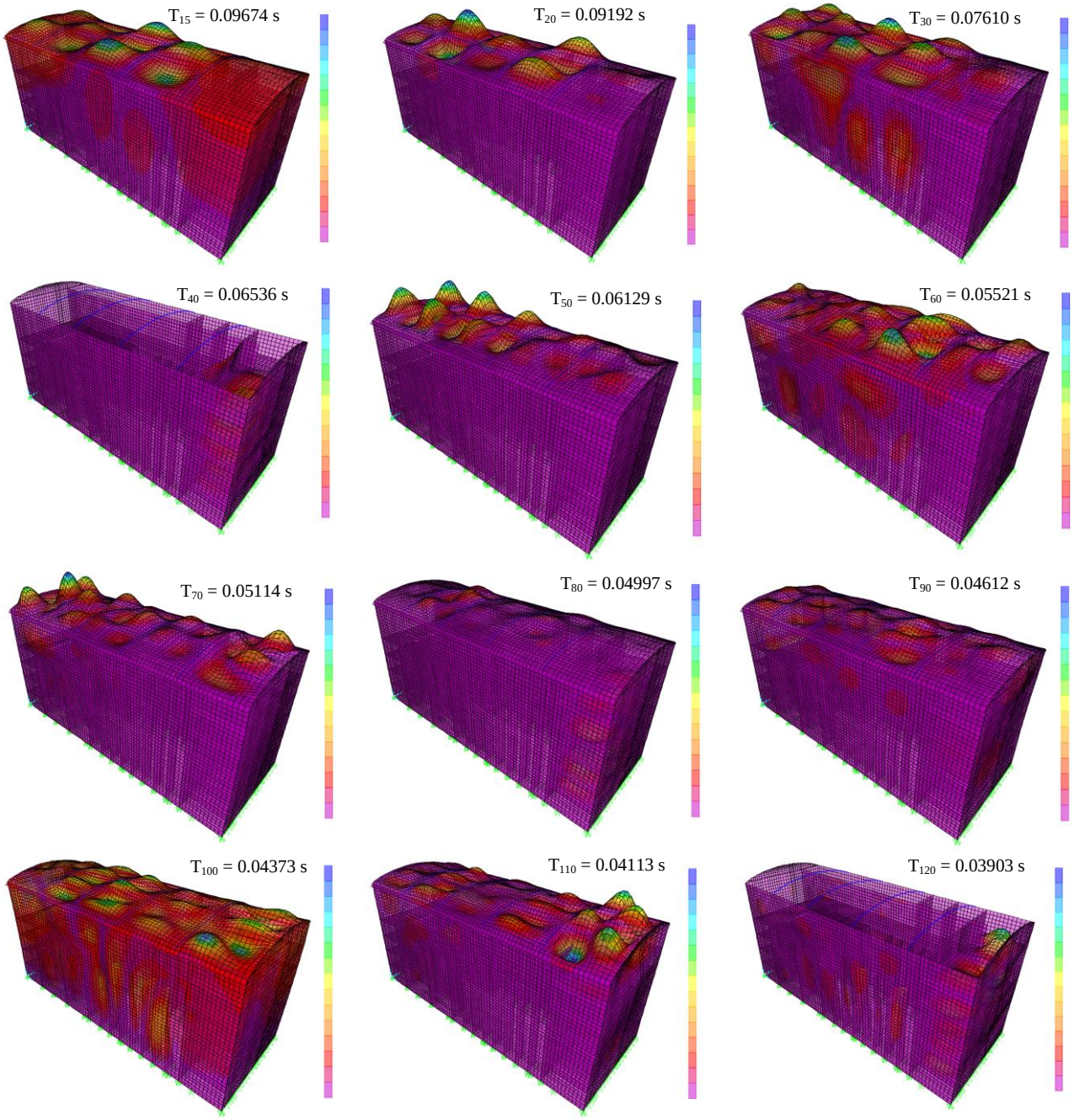

Figure 14 Modal shapes 15, 20, 30, 40, 50, 60, 70, 80, 90, 100, 110 and 120 of the Reactor Building. SAP2000 displacement contours.

Reconan FEA [29] was integrated with an algorithmic implementation to solve large-scale eigenvalue problems and it uses the numerical approach presented in [47], which is known as the Subspace Iteration Method. The initial algorithmic implementation was developed and verified in [48], whereas for the needs of this work the algorithm was optimized so as to be able to handle numerical problems that require more than 64 Gb of RAM. This new algorithmic implementation was used to compute the first 12 fundamental modes of the 3D model presented in Fig. 8, where the obtained results were compared with the results derived from SAP2000. Table 4 shows the comparison between the eigenvalues derived from the two software, where it can be seen that the average difference is 1.99%. The numerical differences are mainly attributed to the stiffness matrix formation that is controlled from the corresponding FE used to discretize the RB. When the shell FEs are combined with the beam-column FE at the roof of the structure, their volumes overlay thus the model is

found to induce parasitic stiffness. In addition, all the connection edges between the shear walls and the slabs (including shear wall to shear wall connections) have overlay volumes that geometrically cannot be separated thus numerically the stiffness overlay is also present adding parasitic local stiffness at those areas. On the other hand, the hexahedral mesh does not suffer from this discretization-related problem given that the exact geometry of the structure is discretized in its exact form. Therefore, the 3D detailed model's numerical results are to be considered more accurate and reliable in this case, even though the computed numerical differences between the two software were found to be small.

Table 4 . Comparison between the first 12 fundamental modes computed by Reconan FEA and SAP2000.

	Reconan FEA		SAP2000		
Mode	f (Hz)	T_R (s)	f (Hz)	T_S (s)	$\frac{T_R - T_S}{T_R}$
1	4.5490	0.2200	4.4342	0.2255	-2.58%
2	4.7340	0.2110	4.9988	0.2001	5.31%
3	5.3680	0.1860	5.7683	0.1734	6.93%
4	6.0030	0.1670	6.6680	0.1500	**9.98%**
5	6.8900	0.1450	6.9454	0.1440	0.80%
6	7.0620	0.1420	7.1129	0.1406	0.72%
7	7.2690	0.1380	8.0548	0.1242	9.76%
8	8.0620	0.1240	8.3472	0.1198	3.41%
9	8.4330	0.1190	8.4225	0.1187	-0.12%
10	8.8710	0.1130	8.4962	0.1177	-4.41%
11	9.0120	0.1110	8.5295	0.1172	-5.66%
12	9.1210	0.1100	9.0984	0.1099	-0.24%
				Average:	1.99%

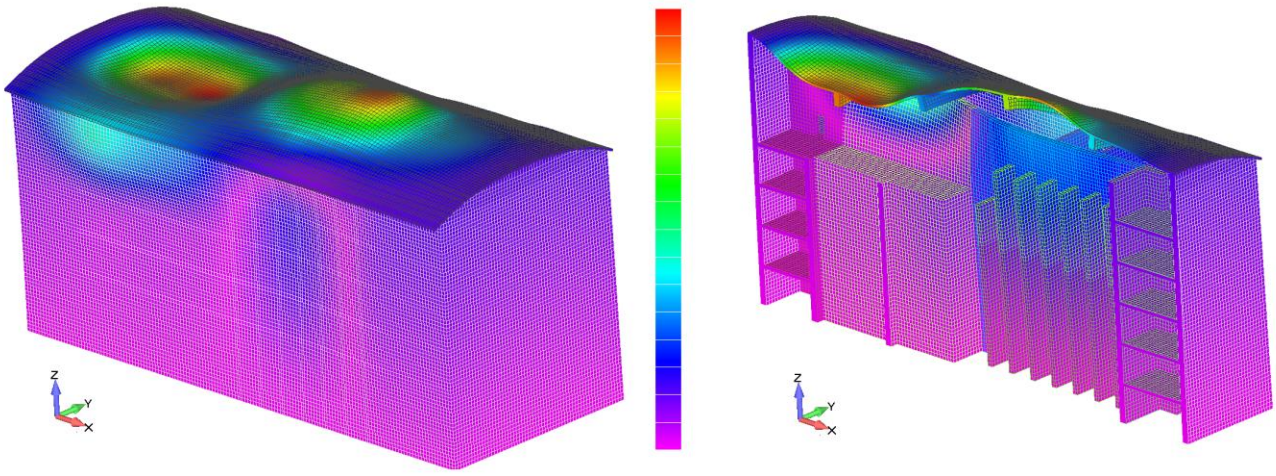

Figure 15 Modal shape 4 (Left) Full 3D view and (Right) Section view. Reconan FEA displacement contours.

Additionally, in order to further compare the numerical results computed by the two FE models, Fig. 15 is provided where the 4th modal shape can be seen, as it resulted from the hexahedral model. As it can be depicted from Table 4, the 4th period is where the largest difference was computed among the 12 numerically resulted modes (9.98%). When Fig. 15 is compared with the corresponding modal shape of Fig. 13 (T_4 = 0.14997 s) it can be seen that the overall computed shapes are similar. It is again imperative to stress out herein the complexity of the at hand numerical problem and the importance of taking into account the fact that shell and

beam-column FEs are not capable of discretizing the exact geometry of the structure thus the numerical difference that derived from this numerical investigation were anticipated.

So as to further validate the numerically obtain results from the modal analysis, the New Greek Seismic Code (NEAK) [40] formula for computing the first fundamental period of a structure (see Eq. 8) was used, given that it takes into account a more objective approach compared to both Eurocode 8 [41] and ACI-318 [42] codes. This is due to the fact that it accounts for the presence of shear walls and the dimension of the structure along the direction of the computed oscillation. In general, international codes use formulas that have a form of $T = C\,H^b$, where C and b are constants, while H is the height of the structure (from the ground level).

$$T_{1,NEAK} = 0.09 \cdot \frac{H}{\sqrt{L}} \sqrt{\frac{H}{H + \rho L}} \tag{8}$$

where H is the total height of the building (from the ground level), L is the dimension of the building along the axis that the period is calculated for, and ρ represents the percentage of the summation of the shear wall areas placed along the direction of the expected oscillation over the total area of the vertical structural members.

Based on the NEAK code [40], the fundamental period along the short dimension of the RB (L = 30 m, ρ = 0.44 and H = 12.5 m), is found to be equal to $T_{1,NEAK}$ = 0.1364 s, which is in a good agreement with the numerically derived fundamental period ($T_{y,SAP2000}$ = 0.1406 s, $T_{y,Reconan}$ = 0.1420 s). According to the modal analysis performed with SAP2000, the highest in frequency computed mode had a period of T_{120} = 0.039 s and the deformed shape consisted of bending of the floor slabs and the reactor walls out-of-plane oscillation. Finally, mode 40 (T_{40} = 0.065 s) derived a deformed shape that consisted of an overall torsion of the building combined with internal shear wall oscillation that foresaw an out-of-plane bending. Despite the relatively large size of the building, the modal analysis shows that the box-shaped geometry provides a relatively high stiffness to the frame that does not allow for large deformations. In addition to that, the fact that the RB is embedded within the soil domain (-25 m) makes this structure exhibit a very stiff behavior due to the surrounding soil that restrains the free deformation of the structure below the surface of the ground. It must be noted here that, the computed modes presented in Figs. 13 and 14 derived by only applying constraints at the raft foundation of the structure.

A second SAP2000 model was developed as well, where the underground retaining walls were restrained from deforming out-of-plane due to the in-situ soil. The modal analysis was performed by using the new boundary condition and it was found that the first 12 modes were similar to those presented in Fig. 13. As it was expected, the resulted behavior of the frame was relatively stiffer, thus the computed modes had lower period values. For instance, the 6th period that consisted the horizontal oscillation along the global y-axis, had a value of T_6' = 0.1202 s which is 14.5% lower than the corresponding period duration computed when the unrestraint model was used. This value is also 11.9% smaller than the corresponding value calculated by using the NEAK formula expressed by Eq. 8. In reality the soil domain will allow the retaining walls to deform and the raft slab to develop deformations thus the overall behavior will be more flexible than the one obtained from the numerically restraint model. Conclusively, the computed modes by using the restraint and unrestraint models represent the upper and lower boundaries of the actual expected response of the structure, in terms of stiffness.

For further validating the hexahedral mesh, the developed 3D detailed model was analyzed so as to compute the deformations and stresses developed due to the operational loads and the lateral soil pressure (Serviceability Load Combination, SLC) whereas the obtained numerical results were compared with those derived from the SAP2000 model that considered the same loads.

Figs. 16 and 17 illustrate the deformed shapes due to the SLC as they resulted from the Reconan and SAP2000 models. It is easy to observe that the maximum deformation resulted at the roof above the spent fuel storage in both models. The asymmetric roof deformation that resulted in both numerical models is attributed to the soil lateral pressure that is applied at the longer retaining walls (North and South), which pushes them inwards

forcing their deformation along the y-axis as illustrated in Figs. 16 and 17 (out-of-plane bending). Especially the South wall that derived the largest deformations along the y-axis, it was found to develop counterclockwise bending moments at the joints where it connects with the four roof beams, caused by its out-of-plane bending. This reaction moments, force the affected joints to uplift the roof beams causing the deflection of the roof that is located above the reactor pool to result into a smaller deflection in comparison to the West part of the roof found above the spent storage tank. The maximum horizontal deformation of the retaining walls was computed to be equal to 1 cm, which was located approximately at the midspan of the South wall.

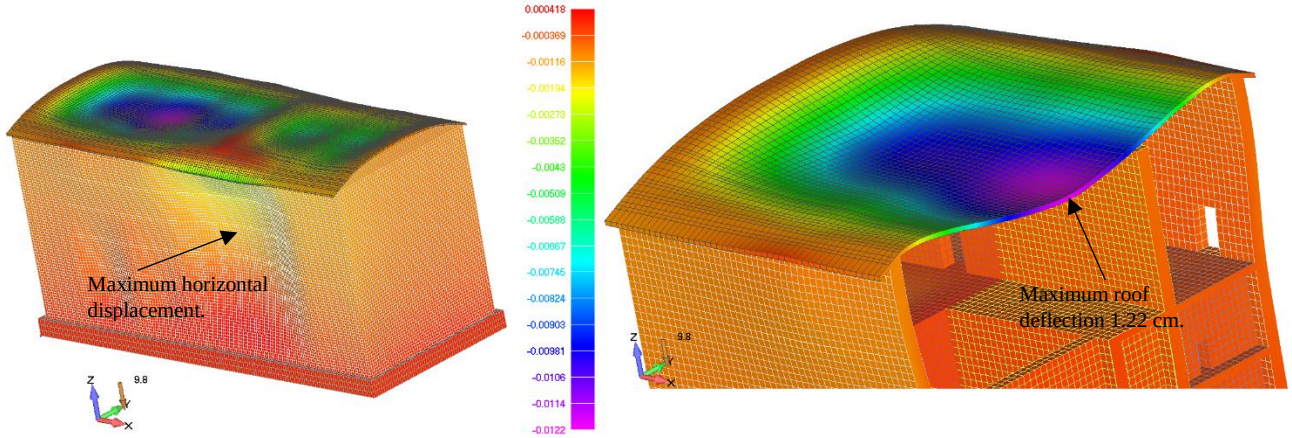

Figure 16 Detailed Model with Fixed Base. Deformed shape due to Serviceability Load Combination. Z-displacements contour.

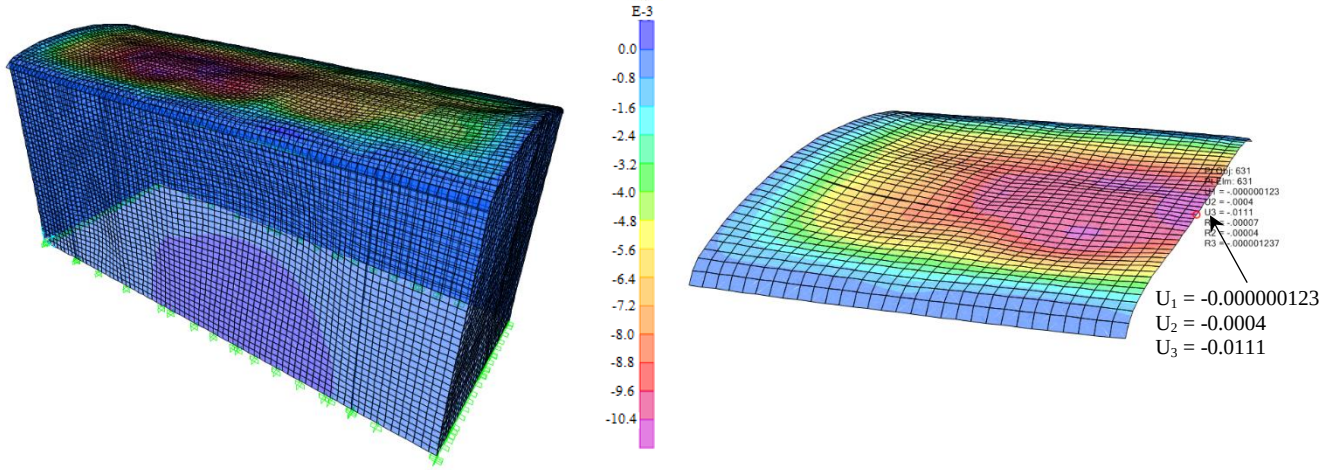

Figure 17 SAP2000 Model. Deformed shape due to Soil Load Combination. Z-displacements contour.

According to the numerical findings, the Reconan model derived a maximum deformation of 1.22 cm at the roof of the RB, with the model that used shell FEs to have resulted a 9% smaller deflection. This numerical finding is attributed to the stiffer behavior of the shell FE in comparison to the hexahedral FE that takes into account the full stress-strain tensors so as to compute the stress state at each Gauss point. The use of beam-column FEs to model the beams within the SAP2000 model also plays an important role inducing a parasitic stiffness given that the 30 cm thick shell FEs that were used to discretize the roof slab are directly connected to the linear elements thus an overlapping of the two different in dimensionality FEs occurs. This is not the case when discretizing the building with hexahedral elements, where the exact geometry is represented in 3D. Finally, the size of the FEs used to discretize the two models was also different thus controlled the numerical outcome. Nevertheless, the two models resulted similar deformation magnitudes, which is a first indication that they are error free.

Figs. 18-20 show the deformed shape and von Mises stress contour as they resulted from the Reconan model. As it can be seen, the main areas of stress development are found at the base of the retaining walls due to the soil lateral pressure and at the joints of the exterior wall with the arch beams (due to the bending moments and the shear forces developed at these structural parts). It must be noted at this point that the stress contours in these figures were leveled by using 10, 18 and 7.5 MPa as maximum von Mises stresses in an attempt to optimally highlight the stress development at each area of the structure. In Fig. 19, which shows the developed stresses by performing a YZ section at the area of the reactor pool, it can be seen that the maximum stress was found to develop at the base of the reactor pool's shear wall that is connected in a perpendicular manner to the South retaining wall that undertakes the soil pressure along the y-direction (this is the area where the maximum horizontal deformation occurs due to the lateral soil pressure). The maximum von Mises stress computed at the base of this reactor's shear wall was computed to be equal to 18,819 kPa, while the maximum von Mises stress developed at the retaining wall was found to be equal to around 6,000 kPa (see Fig. 20).

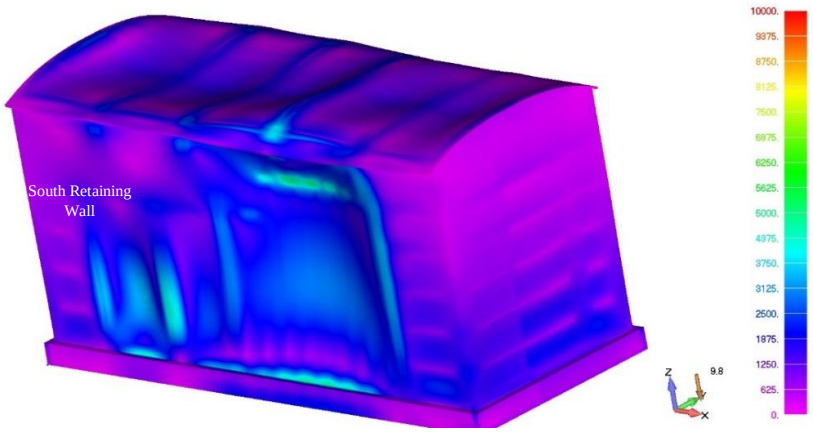

Figure 18 Detailed Model with Fixed Base. Deformed shape due to Serviceability Load Combination. Von Mises contour in kPa. Full 3D view.

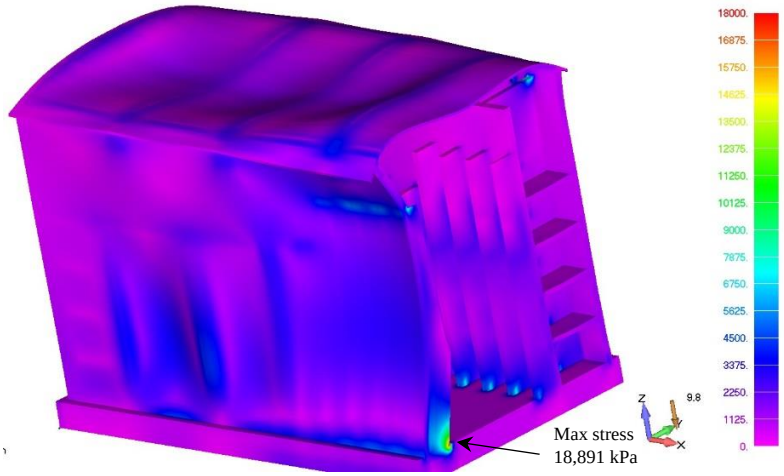

Figure 19 Detailed Model with Fixed Base. Deformed shape due to Serviceability Load Combination. Von Mises contour in kPa. YZ section at the reactor pool.

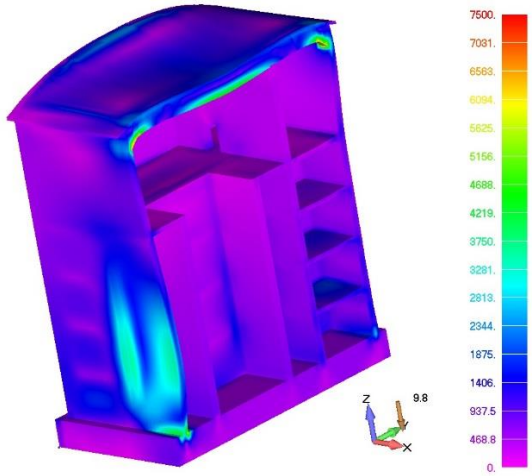

Figure 20 Detailed Model with Fixed Base. Deformed shape due to Serviceability Load Combination. Von Mises contour in kPa. YZ section at the fuel spent storage.

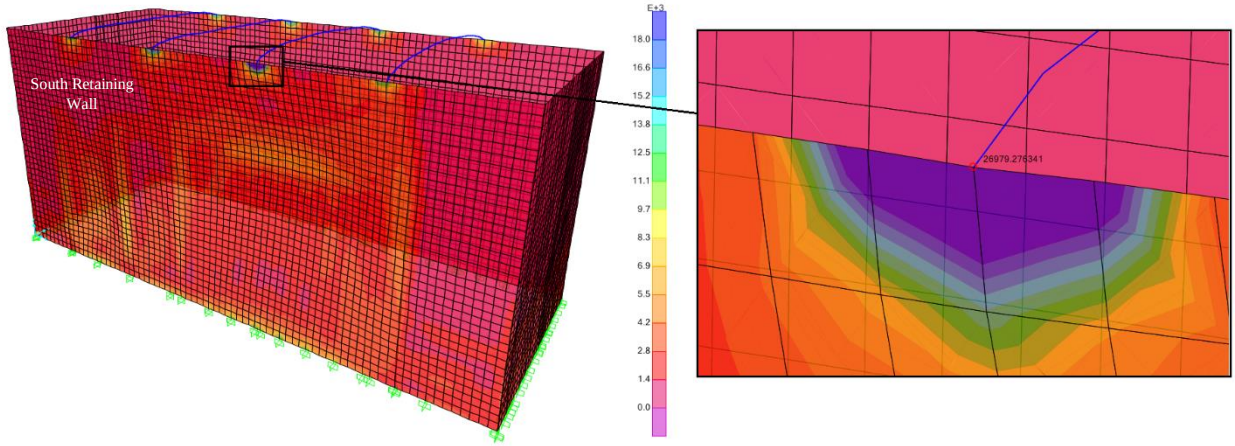

Figure 21 SAP2000 model. Deformed shape due to Serviceability Load Combination. Von Mises contour in kPa. Exterior wall and beam to wall joints.

Fig. 21 shows the corresponding von Mises stress contour of the retaining walls and the joints of the arch beams with the exterior walls of the RB, as it resulted from the SAP2000 model. It is easy to observe that the stress concentrations at the roof joints are significantly larger (max stress 26,979 kPa at the second beam from the right) in comparison to the model that uses solid elements (corresponding max stress based on the solid elements solution: 12,180 kPa), a numerical phenomenon attributed to the mesh and the fact that the beam-column FEs that were used to model the arch beams are connected to the shell mesh at a single node. Through this node, which is also connected to the two shell FEs used to locally discretize the wall, the entire developed bending moment, shear and axial forces are transferred from the beam to the wall, which is the cause of the resulting high local stress concentration [43].

Fig. 22 shows the von Mises stress contour of the South retaining wall and the reactor shear walls that are attached to it in a perpendicular manner, as they resulted from the SAP2000 model. Based on the numerical results the maximum stress was computed to be equal to 22,894 kPa at the base of the shear wall (see Fig. 22). This corresponds to a 21% higher stress magnitude in comparison to the Reconan model, whereas it is developed at the lower right area of the reactor pool shear wall (max stress located at the tip of the shell FE). This is also a difference that is attributed to the FE formulation and the ability of the solid FEs to represent the 3D concrete domain in a realistic manner thus avoiding the development of stress concentrations due to discretization limitations. Nevertheless, the numerical analysis showed that in general the retaining walls, the

internal shear walls, and the slabs derived a stress deviation that was found to be within a 5 to 15% margin, hence their numerical differences are mainly attributed to the different numerical formulation of the FEs used and the mesh size.

It is commonly acceptable that solid FEs are ideal for stress analysis in comparison to the 2D FE, but when it comes to the computational demand and the mesh construction efficiency, the use of shell FEs is by far a more convenient and efficient option. Even though the results that derive from the model that uses solid FEs are more accurate and realistic, the computational time required to solve the same problem with shell FEs was only a few minutes, where for the case of the hexahedral FE model the required time was 2 hours. This is also the main reason why professional Civil Engineers have not yet shifted from using standard modeling approaches to the more accurate solid element.

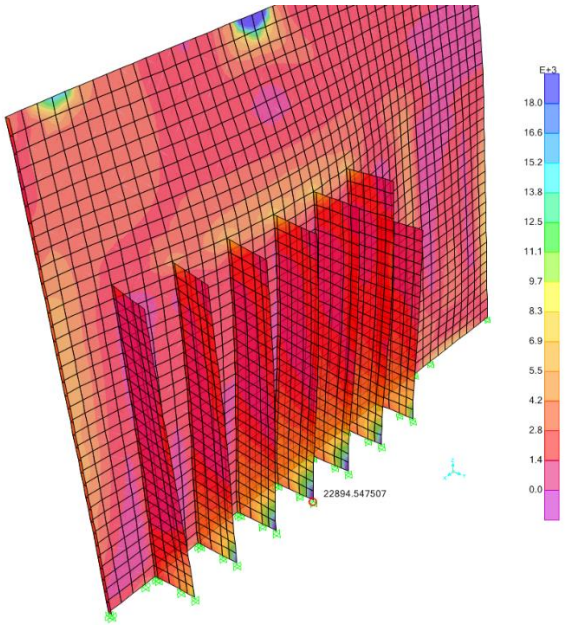

Figure 22 SAP2000 model. Deformed shape due to Serviceability Load Combination. Von Mises contour in kPa. Reactor shear walls and South retaining wall.

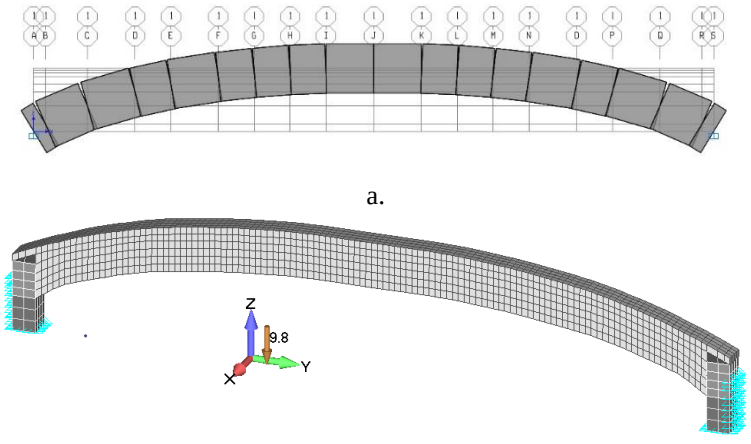

a.

b.

Figure 23 RC arch beam mesh. (a) YZ view of the SAP2000 model with plastic hinges and (b) 3D view of the Reconan model with 20-noded hexahedral and embedded rebar elements.

3.5. RC Arch Beam Assessment

In order to further study the mechanical behavior of the arch beams that are used to support the roof slab, two additional models were developed in SAP2000 and Reconan, respectively, where a nonlinear vertical displacement was applied at the midspan of the beam models. Fig. 23 shows the two models that foresaw the use of beam-column and hexahedral FEs, respectively. The embedded rebar elements of the 3D detailed model (Fig. 23b) can be seen in Fig. 4 found in section 3.1. By using the first FE model, a nonlinear analysis was performed, where it was computed that the maximum vertical resistance of the single arch beam was equal to 68,053 kN and it occurred for a total deflection of 105 mm. It must be noted at this point that, the 30 cm thick roof slab has a total weight that is less than 21,000 kN (this value excludes the self-weight of the four beams' drop). This indicates that the four arch beams have the carrying capacity of withstanding several times the self-weight of the roof slab's weight, while this estimate does not include the carrying capacity of the two exterior shear walls found at the East and West sides of the roof that also support the slab's weight.

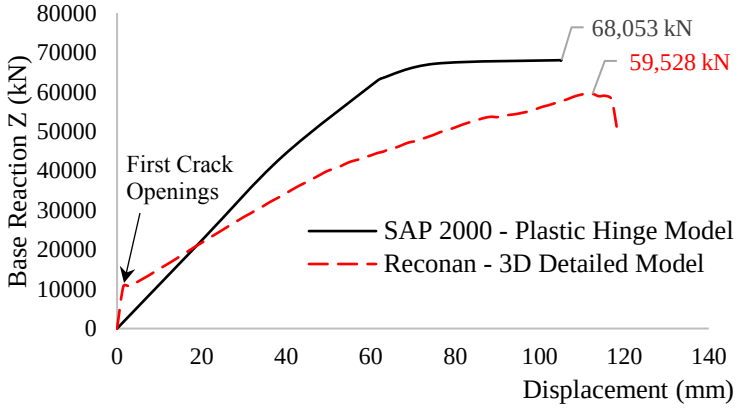

Figure 24 Base reaction vs vertical displacement curves. Comparison between Reconan and SAP 2000 models.

As it can be seen in Fig. 24, the hexahedral model was also solved and the corresponding maximum vertical capacity was found to be equal to 59,528 kN, which represents a 12.5% decreased predicted strength in comparison to the beam-column model. This numerical finding is attributed to the significant effects of the shear strains that occurred during the nonlinear analysis that the simplistic plastic hinge model could not account for. Based on the numerical formulation of the beam-column's plastic hinge, it assumes that the numerical model will derive nonlinearities only in the case when the axial force and bending moments reach the plastic limit based on the law represented in Fig. 5 of section 3.2. Therefore, it fails to capture the significant effect of the shear deformation and the out-of-plane expansion of concrete at the section level, especially at the midspan of the beam where the axial stresses were found to be excessive prior to the arch beam's ultimate limit capacity.

Furthermore, it can be easily observed from Figs. 24 and 25 that the beam-column FE model exhibited a stiffer behavior in comparison to the 3D detailed model, a numerical phenomenon attributed to the numerical inability of the simplistic hinge model to account for the shear strain effect, whereas it fails to account for the corresponding nonlinearities that occur during the analysis. Fig. 25a shows the deformed shape and the plastic hinges that were developed prior to failure when the beam-column FE model was used. The corresponding deformed shapes and von Mises strain contours are also given in the same figure, for comparative reasons, where it is easy to observe the differences between the simplistic and the 3D detailed models. According to the numerical findings obtained through the 3D detailed FE model, the beam-column FE model managed to predict the damages near the supports but failed to capture the actual failure mechanism which foresaw the concrete crashing and rebar failure near the midspan of the beams (see Fig. 25c). The nonlinear analysis resulted a maximum of 7% strain deformation at these critical areas prior to failure. Conclusively, this numerical investigation illustrates the advantages of the 3D detailed method when assessing RC structural

members that are not geometrically simple. It must be noted here that, the same model was used to verify the reinforcement design according to the Eurocode 2 provisions. Based on the design performed in SAP2000, the resulted longitudinal reinforcement was 0.72% at the top and 0.72% at the bottom of the arch beam's section.

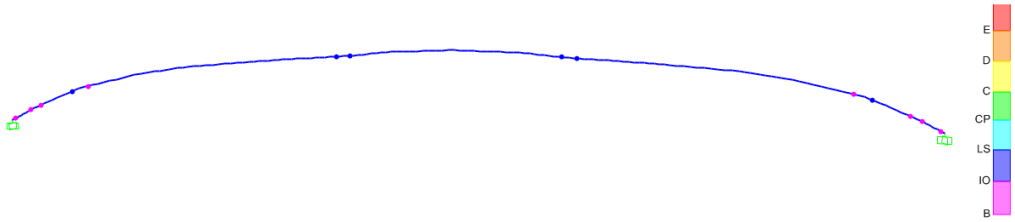

a.

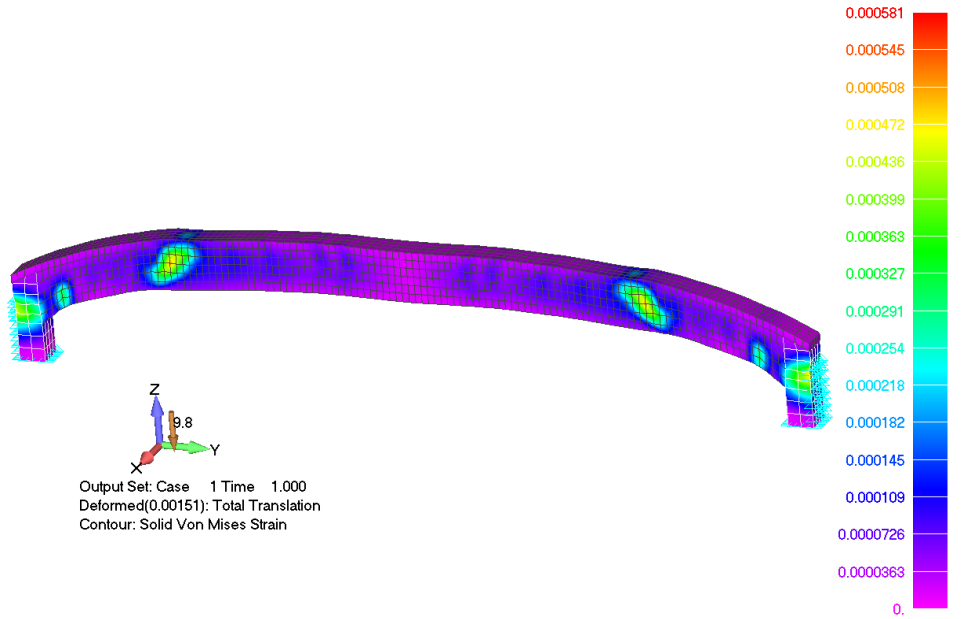

b.

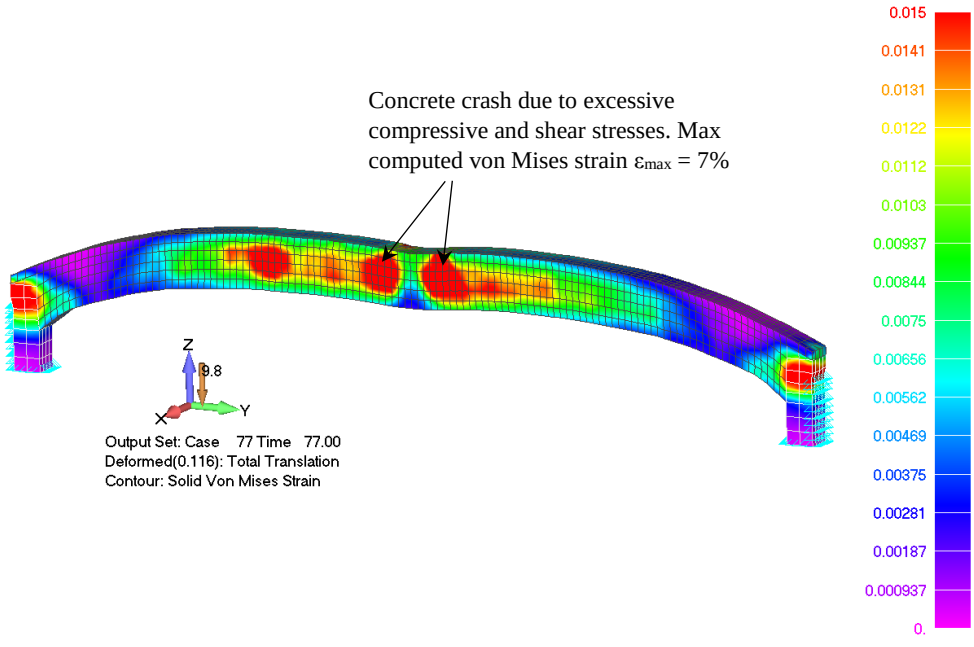

c.

Figure 25 (a) SAP2000 model with developed plastic hinges and deformed shape prior to failure. Reconan model von Mises strains and deformed shape for (b) load step 1 and (c) prior to failure.

3.6. Crack Development due to Operational Loads

Before moving to the analysis of the RB model under seismic loads, Model A was used so as to perform an assessment analysis of the mechanical behavior of the structure for the operational loads, thus investigate whether any cracks might occur. Fig. 26 shows the deformed shape and the crack patterns that were formed at the South retaining wall, as they resulted from the nonlinear analysis. As it can be seen, the lateral soil loads force the South retaining wall to deform horizontally developing a negative bending moment at its base and the support areas where the vertically positioned shear walls are resisting to the horizontal displacement of the retaining wall (see area with vertical cracks in Fig. 26). The relatively flexible behavior of the South retaining wall allows for tensile crack development with a maximum estimated crack width of 0.11 mm. In addition to these cracks, the South wall that acts as a support to the RC arch roof beams developed tensile cracks that had a maximum width of 0.125 mm (see Fig. 26), due to the tensile stresses that were developed at the beam's support.

It is evident that the nonlinear analysis of the RB's framing system by using the 3D detailed modeling approach revealed that the initial design requires to be modified so as to avoid the development of these small in width macro-cracks that resulted due to the flexible behavior of the South retaining wall and the insufficient support of the arch beams that are integrated within the roofing system. Based on these preliminary findings the framing system of the RB was modified accordingly by increasing the thickness of the South retaining wall to 1.5 m (up to the ground surface level), while a RC column with a 150x100 cm section was placed at each arch beam support so as to reassure that the bending moments, shear and axial forces are transferred within the joints without any significant stress concentrations. The South RC wall was also assigned a 150 cm thickness as illustrated in Fig. 27, so as to increase the stiffness of the overall behavior of the South wall behind the reactor pool. It is noteworthy stating at this point that, the selection of an asymmetric RB structural geometry was done intentionally in an attempt to study a more vulnerable structural configuration for the needs of this study. Ideally, a symmetric geometry can be adopted that will foresee the mirroring of the north plan view of Fig. 2 and the addition of 150x100 cm columns at each arch beam support, resulting a structure with sufficient stiffness. The symmetric geometric configuration was also studied in order to establish a spherical understanding of the mechanical behavior of the NuScale structural configuration, but it is not presented in this manuscript for brevity purposes and will be presented and discussed at a later time.

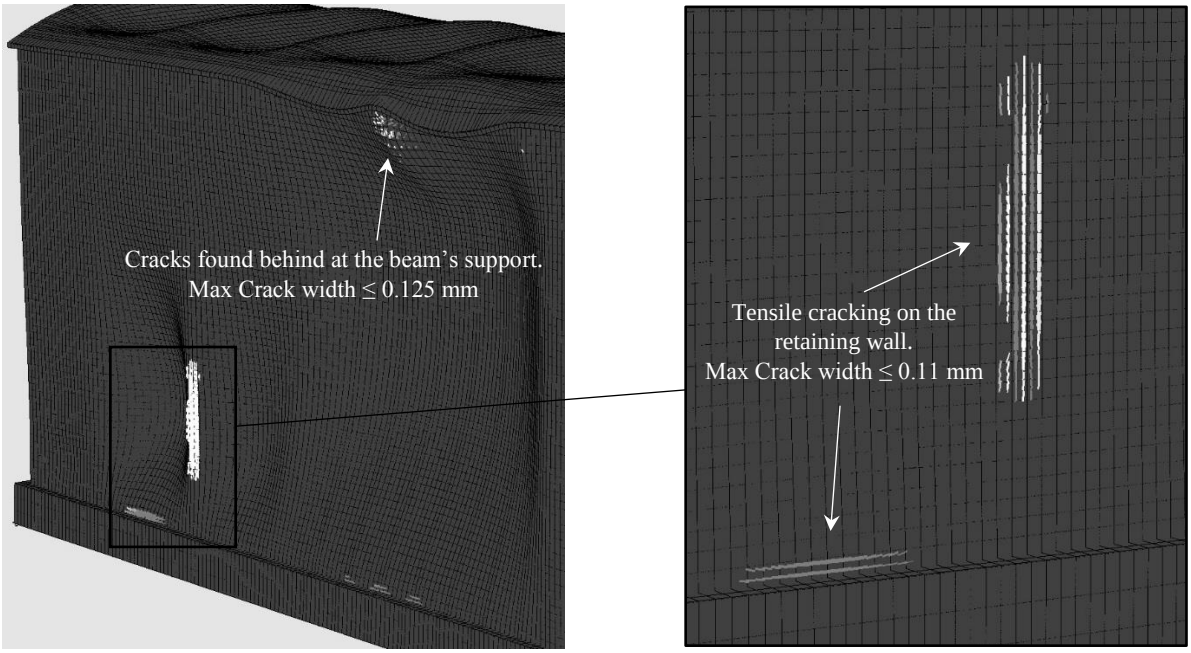

Figure 26 Crack patterns due to the Serviceability Load Combination.

In regards to the steel reinforcement bars used to reinforce the additional columns that can be seen in Fig. 27, a 4.5% reinforcement ratio was used that foresaw the use of 40 mm in diameter flexural steel bars (black colored elements depicted in Fig. 28). Moreover, the new 150 cm thick shear wall that is supported by the South retaining wall, was reinforced with a corresponding 2.83% longitudinal reinforcement ratio (30 mm flexural bars; blue colored elements). After the completion of constructing the additional structural members, the new FE model consisted of 181,076 concrete hexahedrons and 2,703,400 embedded rebar elements. It is noteworthy to mention at this point that, the flexural reinforcement ratio used for the flexural bars found within the RC columns is higher than the maximum allowed reinforcement according to the Eurocode 2 provisions ($\rho_{max} \leq 4\%$) but it is an acceptable ratio based on the ACI318 code. Therefore, in this case the American code is adopted.

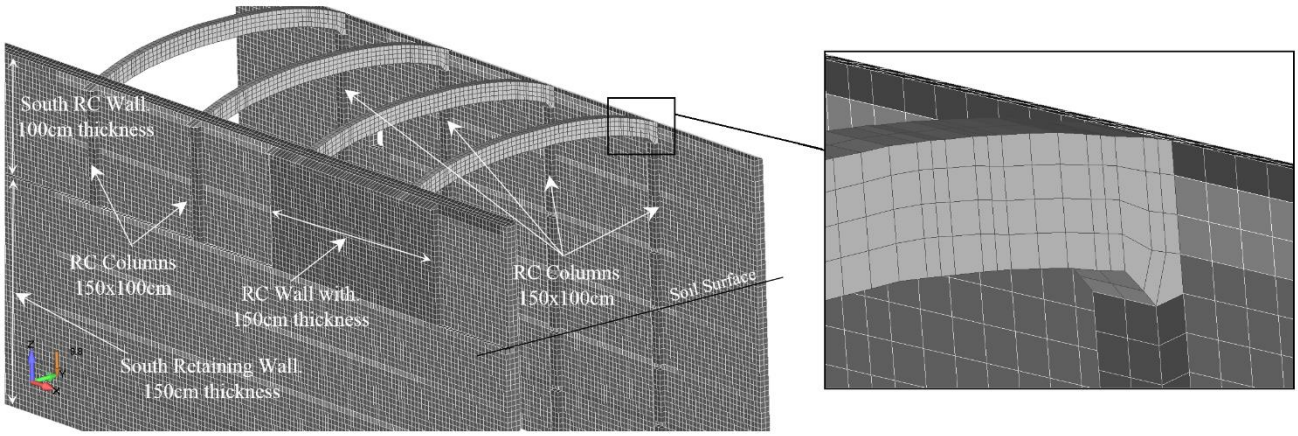

Figure 27 Redesigned RC framing system. Hexahedral mesh.

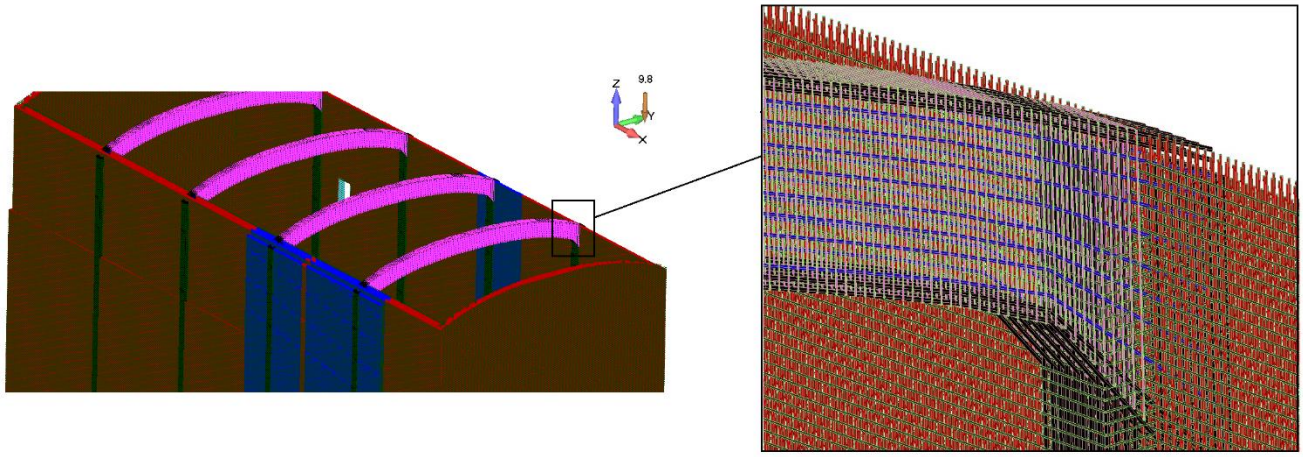

Figure 28 Redesigned RC framing system. Embedded rebar elements of the arch beams, columns and exterior walls.

A new analysis was performed so as to investigate the mechanical behavior of the modified framing system for the SLC in order to re-examine the crack occurrence at the South retaining wall and at the joint of the arch beams with the South RC wall. Fig. 29 shows the new deformed shape of the modified framing system, where it can be seen that the roof slab developed a smaller deflection given that the supporting walls exhibit a stiffer behavior after the increase of the South retaining wall's thickness and the addition of the columns that limited the developed horizontal deformations along the y-axis due to the lateral soil pressure. The y-axis displacement contours can be seen in Fig. 30, where the maximum displacement was computed to be equal to 6 mm at the South retaining wall.

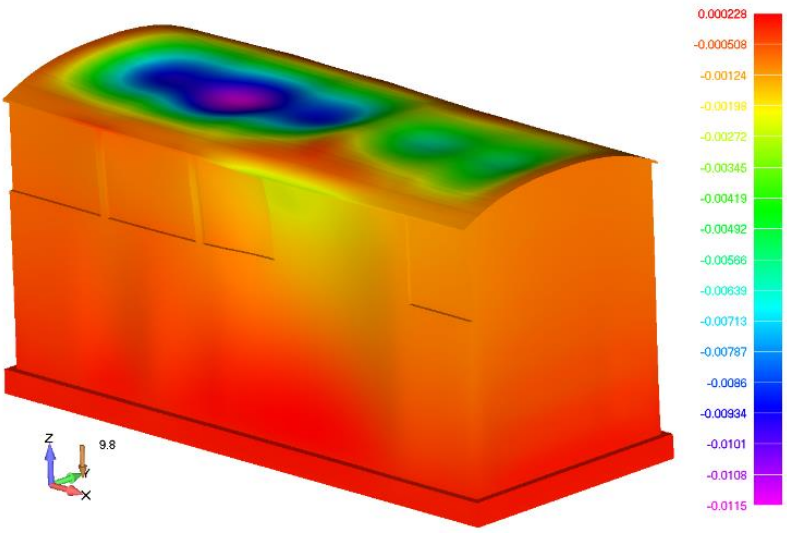

Figure 29 Redesigned RC framing system. Deformed shape due to Serviceability Load Combination. Z-displacements contour.

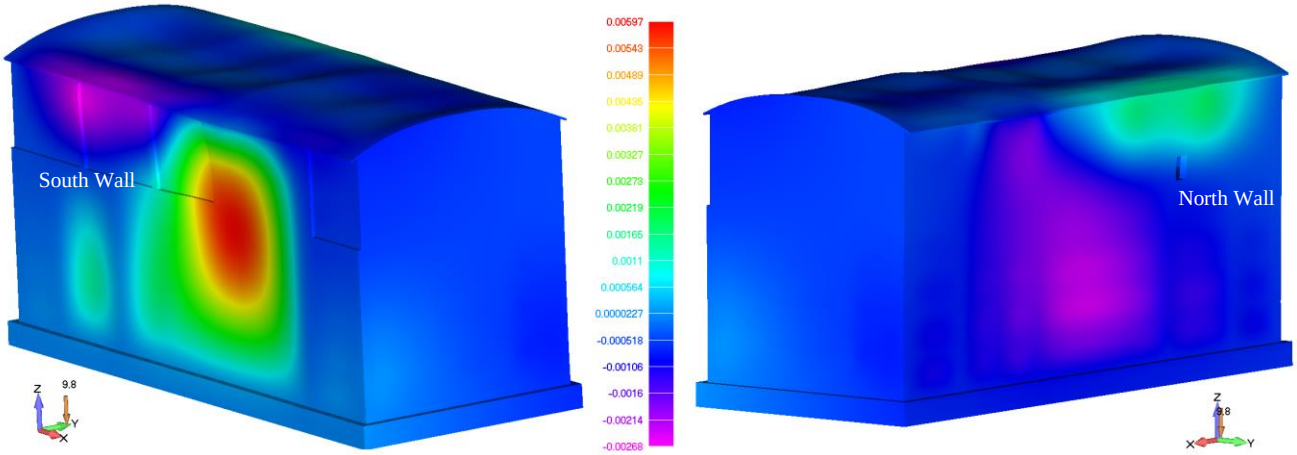

Figure 30 Redesigned RC framing system. Deformed shape due to Serviceability Load Combination. Y-axis displacements contour.

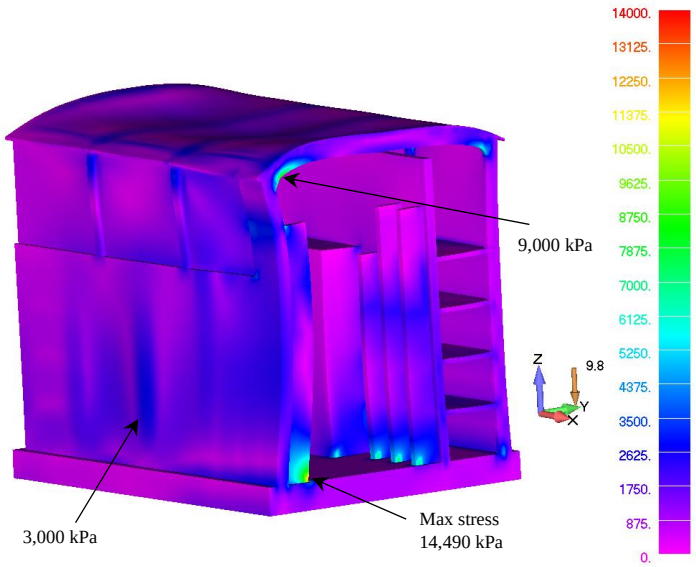

Figure 31 Redesigned RC framing system. Deformed shape due to Serviceability Load Combination. Von Mises contour in kPa. YZ section at the reactor pool.

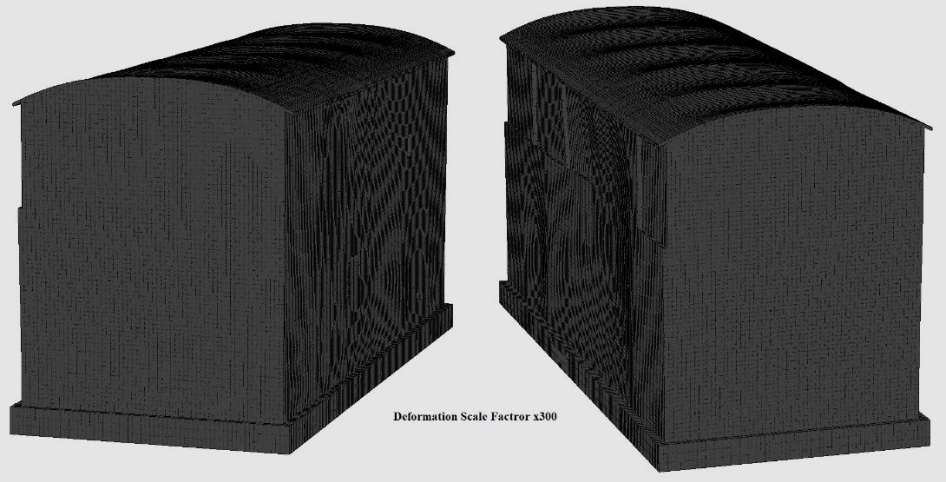

Figure 32 Redesigned RC framing system. Deformed shape and crack pattern of the concrete domain due to Serviceability Load Combination.

The new maximum computed von Mises stress was equal to 14,490 kPa and it was found to develop at one of the reactor pool's shear wall that is connected to the South retaining wall (see Fig. 31). This new stress magnitude constitutes a total of 23.3% decrease in comparison to the stress derived at the initial framing system, while the maximum stress developed at the beam-column joint was found to be equal to 9,000 kPa, as shown in Fig. 31. Furthermore, the maximum stress developed at the South retaining wall was equal to 3,000 kPa, which represents a 50% decrease in comparison to the stress magnitude computed from the initial framing system. This numerical finding is attributed to the increase of the South retaining wall's thickness by 50%. Fig. 32 shows the deformed shape of the 3D detailed model and the corresponding crack pattern, where it can be seen that there were no crack openings on the exterior walls. A partial view of the deform shape of the embedded rebars can be seen in Fig. 33, as it resulted from the numerical analysis. As it can be observed, the embedded rebar mesh follows the deformed shape of the concrete elements.

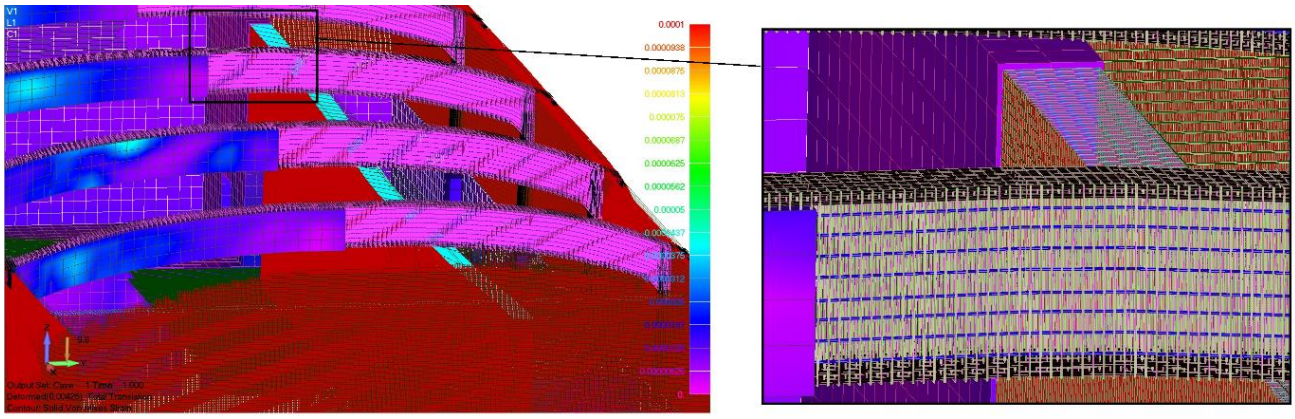

Figure 33 Redesigned RC framing system. Deformed shape of the embedded rebars and solid von Mises strain contour due to Serviceability Load Combination.

From the computational point of view, Table 5 provides the computational times required for the embedded mesh rebar generation and the solution of the equilibrium equations. For the mesh generation of the embedded rebars, the total required time was 51.75 minutes for the case of the initial framing system, whereas the corresponding mesh generation time for the modified model was 54.14 minutes. The computational times correspond to the generation of 2,530,843 and 2,793,400 embedded rebars, respectively. The corresponding solution time for the initial model was 5.14 hours for 2 internal iterations and 2.58 hours for 1 internal iteration for the case of the redesigned framing system. The initial model required a 2nd internal iteration to converge due to the crack openings that released unbalanced forces during the Newton-Raphson iterative procedure. It

must be noted here that the CPU that was used to run the analyses had a computational capacity of 4.20 GHz per core.

Table 5 Numerical details and computational time for the solution of the 3D detailed models.

Model	Stiffness Matrix Size (Gb)	Number of Dofs	Number of Embedded Rebars	Embedded Rebar Generation time (minutes)	Internal Iterations Solved	Solution Time (hours)
Initial	35	754,563	2,530,843	51.75*	2	5.14**
Redesigned	35	792,690	2,703,400	54.14*	1	2.58**

*Parallel processing with the use of 8 cores.
**Serial processing.

3.7. Soil-Structure Interaction Analysis

Model B (see Fig. 11), which foresaw the discretization of the soil domain through 8-noded hexahedral elements, was used so as to investigate the expected settlement of the RB due to the loads applied on the structure during operation, while the maximum developed stresses at the soil level was also examined. The redesigned building was used herein so as to discretize and analyze the structural behavior of the RB within Model B, where the mesh details of the model can be found in Table 2. Two main analyses are presented in this section, which aim to investigate the magnitude of the maximum stress developed at the soil level (found under the raft foundation) and check the differential settlement of the raft foundation when the reactor pool is operating at a 50% capacity. Meaning that only 6 NRMs will be assumed to be operating within the reactor pool thus the loads applied on the South reactor wall will be higher than the North side of the building, where the NRMs reactor hosting areas are assumed to be empty. This is a load distribution scenario that can lead to a differential settlement of the raft foundation.

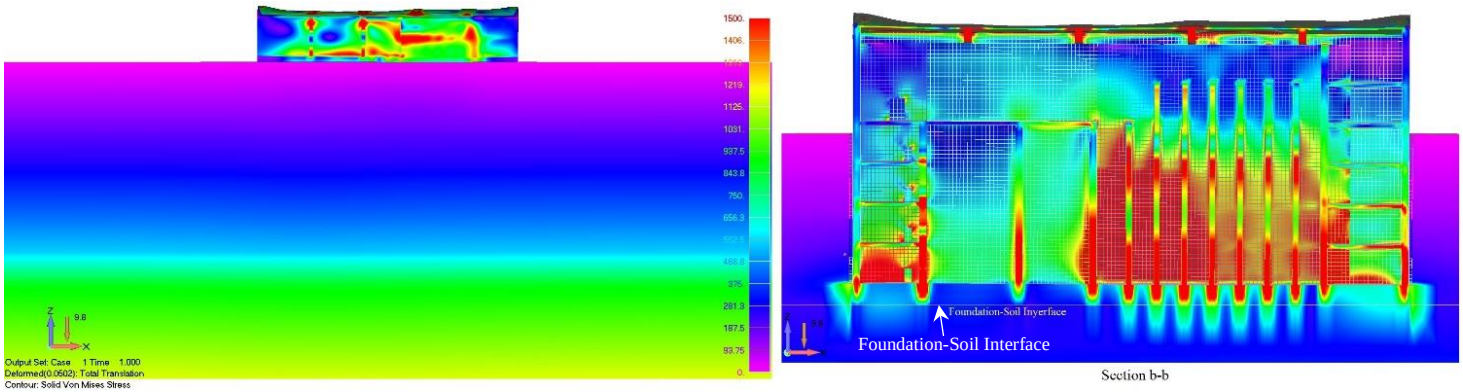

Figure 34 Model B (SSI). Von Mises stress contour in kPa due to the Serviceability Load Combination. All NRM present.

Fig. 34 shows the von Mises stress contour of the structure and the soil domain as it resulted from the analysis of Model B, when all NRM were assumed to be present. As it can be seen the stress distribution foresees the development of the maximum stresses at the shear walls where the superstructure loads reach the raft foundation. The transfer of these loads to the soil (through the foundation-soil interface) generates the stress pattern shown in Fig. 35, where the maximum computed stress was equal to 700 kPa (less than the maximum soil strength) and was found to develop under the reactor shear walls located at the South wall. Fig. 36 shows the deformed shape of the soil domain by using a scaled factor of x500, where it can be seen that the South wall developed a larger settlement due to the load distribution that is higher at that area because of the NRMs and the presence of the thicker retaining wall. It must be noted at this stage that, the maximum settlement recorded at the foundation level was equal to 39.2 mm, which does not constitute any structural problems to the frame's integrity due to excessive deformations of the soil. This numerical finding is only valid for the specific under study geological profile.

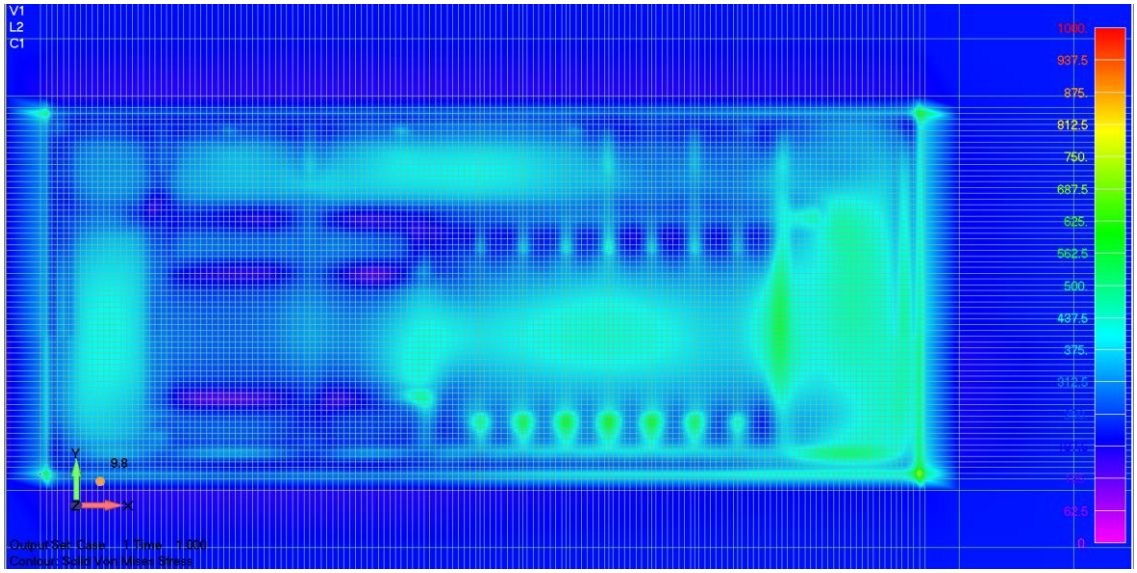

Figure 35 Model B (SSI). Von Mises stress contour in kPa due to the Serviceability Load Combination. Foundation-soil interface. All NRM present.

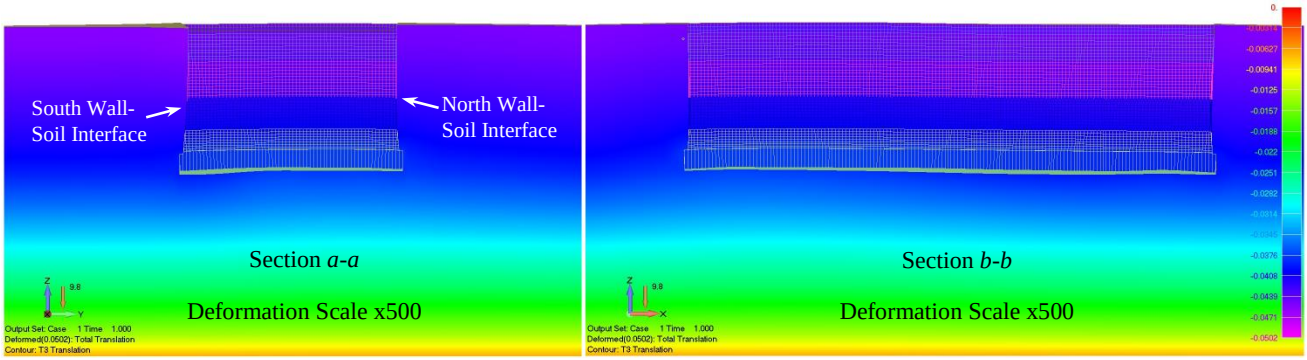

Figure 36 Model B (SSI). Soil domain deformed shape and z-axis displacement contour due to the Serviceability Load Combination. All NRM present.

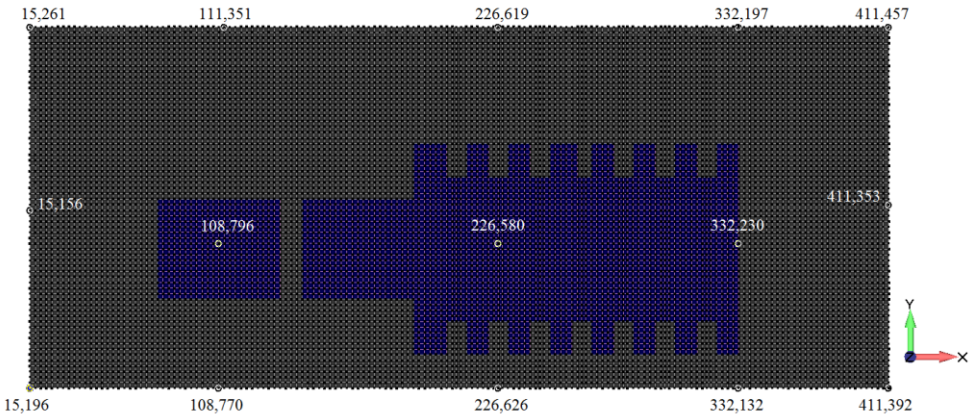

Figure 37 Model B (SSI). Nodes located on the raft foundation that were used to record the RB's settlement.

The settlement of RB was monitored at 15 nodes that were located on the raft foundation as shown in Fig. 37. After the completion of the second analysis by using Model B and the load combination that foresaw that the RB was operating with 6 out of the 12 NRMs located at the South area of the reactor pool, the new settlements were recorded and are given in Table 6. As it derived from the new SSI analysis, the overall settlement was smaller due to the decreased applied dead loads, but the corresponding differential settlement was larger for the

case of the new load distribution. Table 6 shows the rotations of the raft foundation at different locations along the global x-axis that were numerically computed for the two loading scenarios described above. As it can be observed, even though the increase of the raft foundation's rotation was 30% in some locations (for the second loading scenario), the overall rotation of the slab was very small. This mechanical behavior is attributed to the fact that 65% of the RB is found underground, a structural feature that provides the plant with sufficient stiffness and the ability to transfer safely the superstructure loads to the soil domain without developing significant settlement or stress concentrations.

Table 6 Settlement due to Serviceability Load Combination for the case of 12 and 6 NRM.

Node ID	Load 12 NMRs Settlement δ_{12} (mm)	Load 6 NMRs Settlement δ_6 (mm)	Difference $(\delta_{12} - \delta_6) / \delta_{12}$
15,196	38.7	38.6	0.2%
15,156	37.8	37.7	0.4%
15,261	38.3	38.2	0.4%
108,770	38.3	38.0	0.6%
108,796	37.4	37.0	1.0%
111,351	37.7	37.3	1.1%
226,626	39.2	38.9	0.8%
226,580	37.9	37.2	1.9%
226,619	38.1	37.3	2.1%
332,132	39.5	39.0	1.2%
332,230	38.5	37.8	2.0%
332,197	38.6	37.8	2.2%
411,392	39.8	39.4	1.0%
411,353	38.9	38.4	1.3%
411,457	39.2	38.7	1.4%

Table 7 Raft foundation's rotation due to Serviceability Load Combination for the case of 12 and 6 NRM.

Side	Load 12 NMRs		Load 6 NMRs		Difference $\frac{(\theta^o_{12} - \theta^o_6)}{\theta^o_{12}}$
	Rotation (Rad_{12})	Rotation θ^o_{12}	Rotation (Rad_6)	Rotation θ^o_6	
15,261-15,196	1.13×10^{-5}	6.46×10^{-4}	1.34×10^{-5}	7.70×10^{-4}	16.1%
111,351-108,770	1.89×10^{-5}	1.08×10^{-3}	2.51×10^{-5}	1.44×10^{-3}	24.6%
226,619-226,626	3.51×10^{-5}	2.01×10^{-3}	5.06×10^{-5}	2.90×10^{-3}	30.5%
332,197-332,132	2.98×10^{-5}	1.71×10^{-3}	4.27×10^{-5}	2.44×10^{-3}	30.2%
411,457-411,392	1.94×10^{-5}	1.11×10^{-3}	2.48×10^{-5}	1.42×10^{-3}	21.7%

3.8 Seismic Analysis with Soil-Structure Interaction Considerations

The last set of analyses that will be presented in this work refers to the seismic analysis performed by using Model B that foresees the discretization of the soil domain through the use of 8-noded isoparametric hexahedral FEs in order to consider for the SSI effect. Based on Alicia et al. [44], the epicenter of the earthquake was located on the coast, approximately 8 km West of Curanipe and 115 km North-Northeast of Concepcion, the second largest city of Chile. This earthquake, which is the second strongest in magnitude of Chile's seismic history, was one of the strongest ever recorded and one of the main reasons for why the country did not proceed with its nuclear plant strategy.

The 2010 earthquake was also felt at Valparaiso, Santiago and Araucania, which are cities that accommodate 80% of the Chilean population [44]. Boroschek and Contreras [45] presented the strong ground motion that was recorded during the 2010 Chile earthquake, where they reported a maximum recorded peak ground acceleration (PGA) of 0.93g and a corresponding 5% damped peak structural acceleration (PSa) of 1.73g for structures with a period of 0.1 seconds. Additionally, it was reported that the earthquake affected structures that had 5 or more floors and among the most notable failures that was recorded was that of the collapse of a 12-storey RC building in Concepcion.

In order to study the behavior of the RB under these extreme loading conditions, Model B was used so as to run the corresponding analyses for the seismic assessment of the framing system when it undergoes a 1.73g acceleration. As suggested in [46], Eurocode 8 was used so as to compute the seismic load applied on the building. The load was computed based on a spectrum acceleration of 1.73g. Eurocode 8 foresees the use of the ground acceleration a_g and based on the ground type, and the structure's fundamental period, the elastic S_E (T) and design S_d (T) spectrum accelerations are computed. Table 8 shows the parameters adopted herein so as to achieve an elastic spectrum acceleration of 1.732g and the corresponding seismic force that derived according to the structural mass that is expected to be activated during the dynamic excitation.

As it can be depicted from Table 7, when a ground acceleration a_g = 0.6g is used with a ground type B and a behavior factor q = 1, an elastic spectrum acceleration S_E (T) = 1.732g is obtained, which is in line to the maximum reported PSa for structures with a fundamental period of 0.1 seconds, found in [45]. The fundamental period that was used to compute the elastic spectrum response acceleration, in Table 7, was the one obtained from the SAP2000 model, as it was presented in section 3.4 of this manuscript. The corresponding design spectrum acceleration S_d (T), based on Eurocode 8, was found to be equal to 0.874g by assuming a behavior factor q equal to 2. This assumption foresees that the structure will develop damages during the earthquake thus behave in a ductile manner given an appropriate reinforcement.

The design approach adopted herein requires the structure to be able to withstand safely the effects of a safe shutdown earthquake (SSE) and limit the expected damages to the minimum. For this reason, the seismic load that results when the elastic response spectrum acceleration is considered, where it was applied along the positive and negative y-axis directions in order to study the mechanical response of the NuScale building. The horizontal load was distributed along the height of the structure based on the mass distribution of the building [41], while the dead and 30% of the live loads were applied within the corresponding earthquake load combination [41]. For distributing the seismic loads, the mass of each floor was computed and based on the floor height the loads were applied. The horizontal static equivalent load that was distributed at the nodes of each NuScale floor was 261,793 kN, as it can be found in Table 8 ($F_{E,total}$). It must be noted at this point that, the x-axis direction is not discussed in this work for brevity reasons. In addition to that, the study of the vertical component of the earthquake excitation will not be discussed herein either.

Table 8 Eurocode 8 seismic parameters and computed loads.

Mass Above Ground Level	151,147.9 kN / g		
$T_{1,y\text{-}axis,FEA}$	0.1406 s		
S (ground type B)	1.2		
a_g	0.6g		
T_B	0.15 s		
η	1		
Elastic Response		Nonlinear Response	
q	1	q	2
S_E (T)	1.732g	S_d (T)	0.874g
$F_{E,total}$	261,793 kN	$F_{d,total}$	132,038 kN

Fig. 38 illustrates the deformed shape and the von Mises stress contour that resulted from the numerical analysis of Model B, by assuming that the seismic loads are applied along the positive y-axis direction. The numerical analysis revealed that the solid von Mises stress levels within the framing system did not exceed that of 20,185 kPa, while the structure was found to behave in a rather stiff manner as it can be seen in Fig. 39, where the deformed shape and the y-axis displacement contour are illustrated. The maximum resulted horizontal displacement was equal to 30 mm at the middle of the RB, where the South wall meets with the roof slab. Furthermore, the two shear walls (East and West exterior walls, see Fig. 39) that were parallel to the applied load exhibited a very stiff behavior, while the North and South walls developed an out-of-plane bending exhibiting a more flexible mechanical behavior. Fig. 40 illustrates the resulted von Mises stress contour at the foundation-soil interface, where it can be observed that the maximum developed stresses do not

exceed the magnitude of 1,200 kPa, which is lower than the maximum soil capacity of the corresponding soil layer assumed under the raft foundation level (f_u = 1,500 kPa). The deformed shape of the soil domain can be also seen in Fig. 41, where the resulted deformation is visualized through sections *a-a* and *b-b*, and the differential settlement is visualized by using a scale factor of x300.

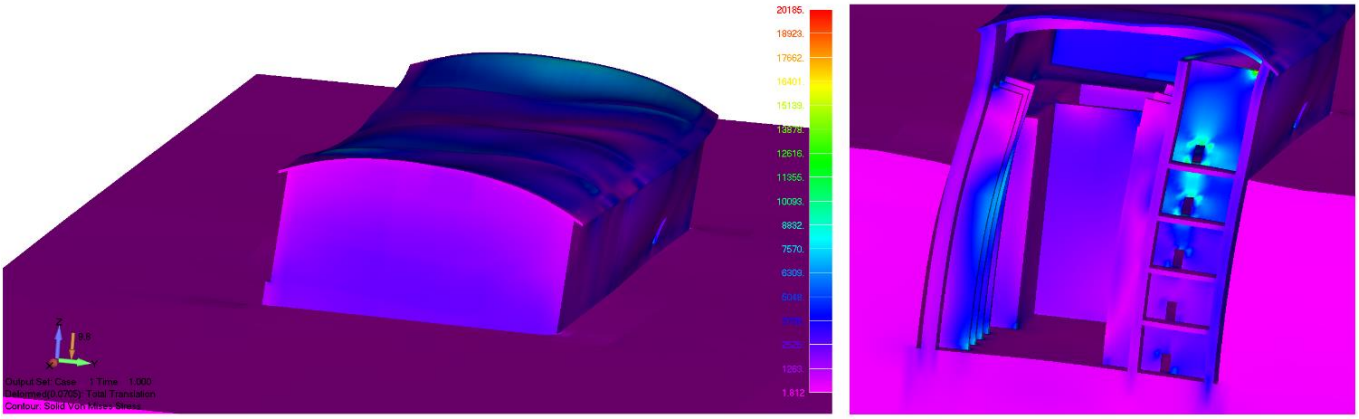

Figure 38 Model B (SSI). Deformed shape and von Mises stress contour due to the SSE loads along the positive y-axis.

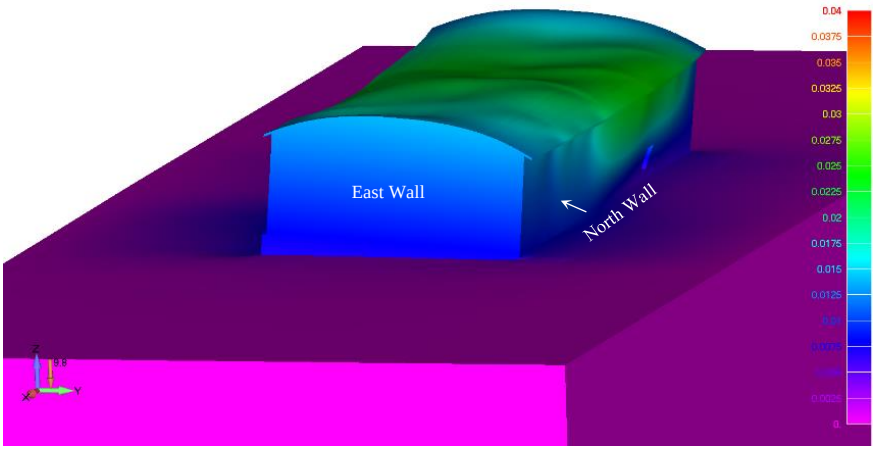

Figure 39 Model B (SSI). Deformed shape and y-axis displacement contour due to the SSE loads along the positive y-axis.

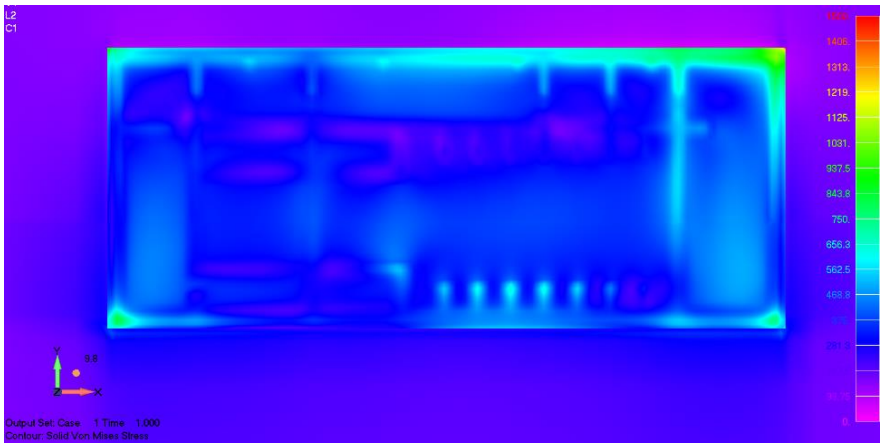

Figure 40 Model B (SSI). Von Mises stress contour on the foundation-soil interface due to the SSE loads along the positive y-axis.

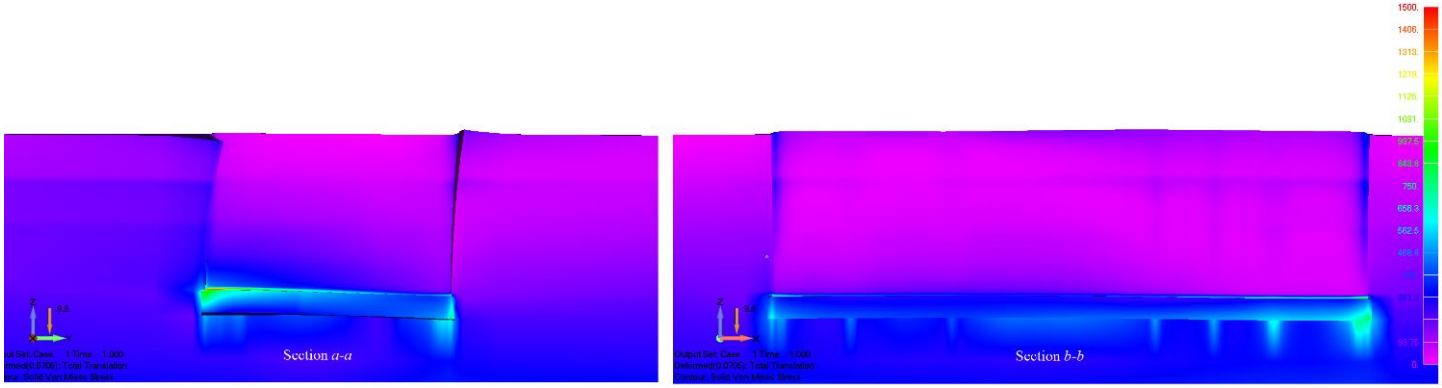

Figure 41 Model B (SSI). Von Mises stress contour in kPa and deformed shape of the soil domain due to the SSE loads along the positive y-axis.

In order to further study the corresponding mechanical behavior of the RB along its weak axis, the same seismic loads were applied along the negative y-axis direction and the nonlinear analysis was performed again. As it resulted from the analysis, the framing system did not develop any plastifications, thus the maximum computed stress within the RC building was found to be equal to 24,000 kPa at the interior shear walls of the structure located near the maintenance area. Nevertheless, this does not constitute that the frame of the structure will not develop any cracks, as it was shown in section 3.6, hence an analysis through the use of the 3D detailed model has to be performed in allocating the main areas where cracks will form due to the seismic load combination. Given that the estimated required RAM for performing such an analysis foresees the use of a PC with a 128 Gb memory, this is currently a task that will be performed in the near future.

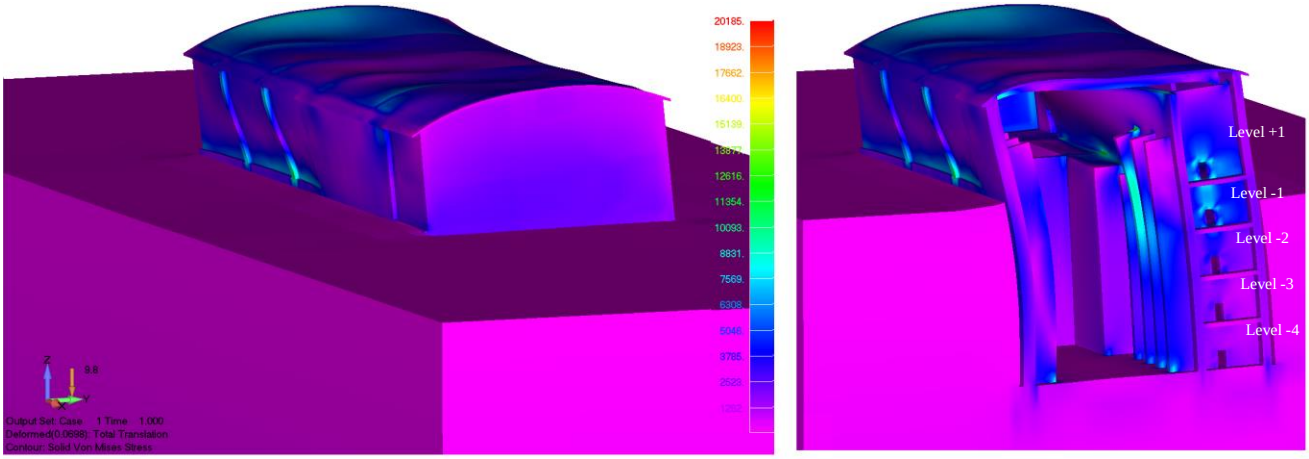

Figure 42 Model B (SSI). Deformed shape and von Mises stress contour in kPa due to the SSE loads along the negative y-axis.

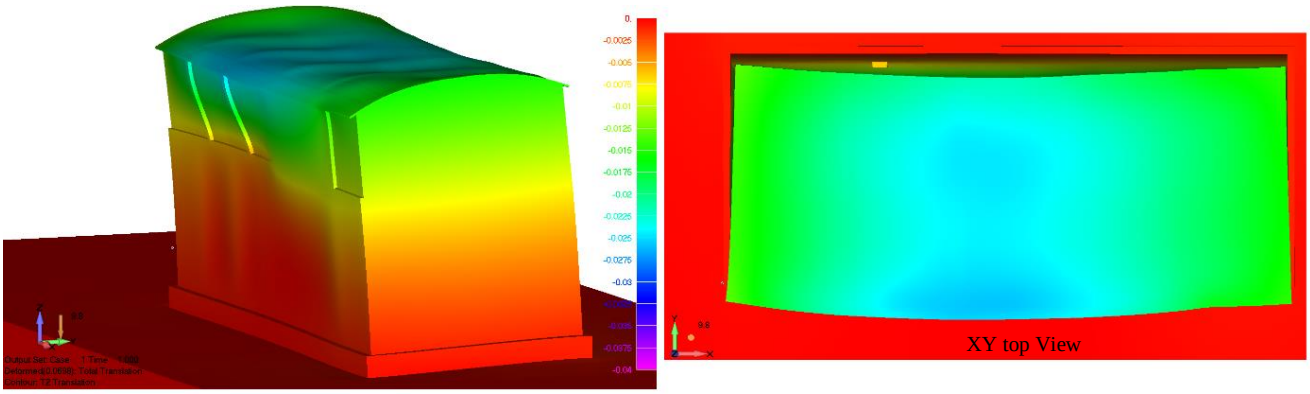

Figure 43 Model B (SSI). Deformed shape and y-axis displacement contour due to the SSE loads along the negative y-axis.

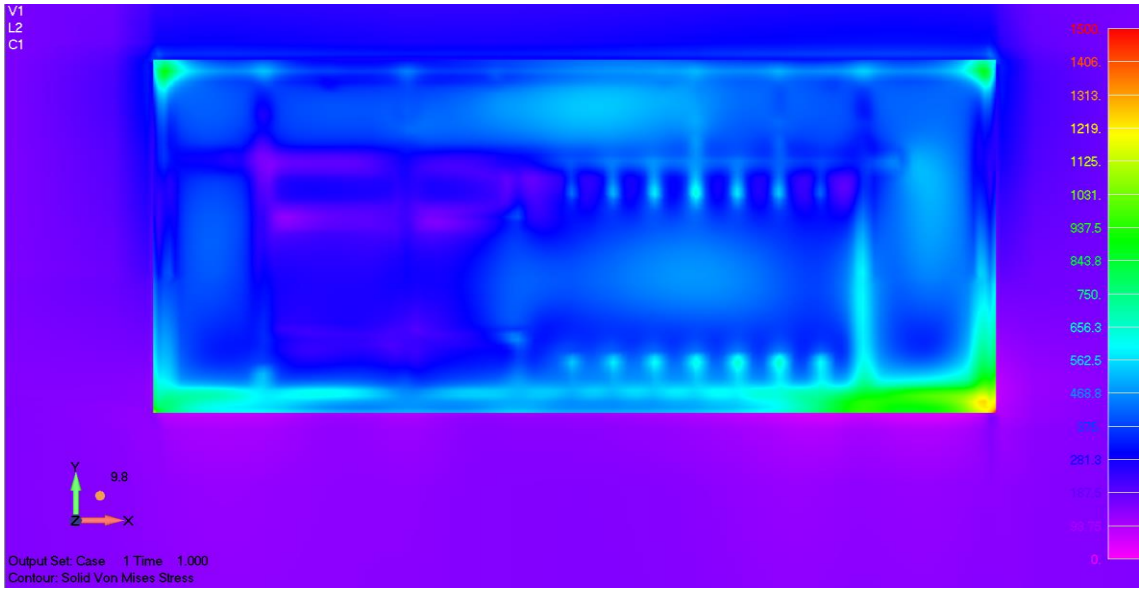

Figure 44 Model B (SSI). Von Mises stress contour in kPa developed on the foundation-soil interface due to the SSE loads along the negative y-axis.

Fig. 42 shows the von Mises stress contour, with a maximum contour level set to 20,185 kPa in order to have the same scale as that used in Fig. 38. An interesting observation that resulted from the two analyses outputs presented through Figs. 38 and 42, is the stress distribution that was computed at the shear wall which is perpendicular to the North exterior wall. The wall was found to develop higher stress magnitudes at levels +1 and -1 due to the seismic loads, while the same shear wall did not develop significant stresses at levels -2, -3 and -4. This highlights the mechanical contribution of the soil and how it affects the structure's overall mechanical behavior when loaded along the y-axis directions (positive and negative). Fig. 43 shows the deformed shape and the y-axis displacement contours as they resulted from the numerical analysis, where it is easy to observe that the overall mechanical behavior of the structure is similar to that presented in Fig. 39. The maximum horizontal displacement was developed at the roof slab at the area where the South wall connects with the roof slab. Furthermore, the deformation shape of the RB from an XY top view is also shown (Fig. 43), where the overall structural out-of-plane bending-like deformation can be observed. Finally, the corresponding von Mises stresses computed at the soil-raft foundation interface are given in Fig. 44, where it can be seen that the maximum computed soil von Mises stress was equal to 1,350 kPa at the Southeast corner of the raft slab.

The overall rotations of the structure were computed based on the settlements found in Table 9, as they resulted from the two push-over analyses. Based on the computed settlement magnitudes given in Table 9, it is easy to conclude that the raft foundation did not exhibit any uplifts, while the maximum settlement was found to be equal 42.5 mm at node 411,392 (see Fig. 37) for the case where the SSE loads faced the negative y-axis horizontal direction. It is also easy to observe from Table 10 that, the soil profile that was assumed in combination with the sitting configuration of the building do not allow the structure to develop any significant rotations thus the overall computed deformations of the framing system do not pose any problems to the integrity of the RB. Given that the previous analyses foresaw that the soil's water table was below the raft foundation, two more analyses were performed so as to investigate the overall mechanical behavior of the RB, when buoyancy forces are accounted for.

Table 9 Settlement due to the SSE loads for the cases of positive and negative y-axis directions.

Index	Node ID	Load +y axis Settlement δ_{+y} (mm)	Load -y axis Settlement δ_{-y} (mm)	Load +y axis & buoyancy Settlement $\delta_{+y,b}$ (mm)	Load -y axis & buoyancy Settlement $\delta_{-y,b}$ (mm)	$\frac{\delta_{+y}-\delta_{+y,b}}{\delta_{+y}}$	$\frac{\delta_{-y}-\delta_{-y,b}}{\delta_{-y}}$
1	15,196	36.5	40.8	33.3	37.6	8.8%	7.8%
2	15,156	37.8	37.9	33.9	34.0	10.3%	10.3%
3	15,261	40.4	36.2	37.2	33.0	7.9%	8.8%
4	108,770	36.0	40.5	31.6	36.1	12.2%	10.9%
5	108,796	36.8	38.0	31.3	32.5	14.9%	14.5%
6	111,351	39.9	35.5	35.6	31.1	10.8%	12.4%
7	226,626	37.6	40.8	33.0	36.2	12.2%	11.3%
8	226,580	37.2	38.6	30.8	32.2	**17.2%**	**16.6%**
9	226,619	40.2	36.0	35.6	31.4	11.4%	12.8%
10	332,132	36.6	42.4	32.2	38.0	12.0%	10.5%
11	332,230	37.7	39.4	32.2	33.9	14.6%	14.0%
12	332,197	41.6	35.6	37.2	31.2	10.6%	12.4%
13	411,392	37.1	**42.5**	33.8	**39.2**	8.9%	7.8%
14	411,353	38.9	38.8	35.1	35.0	9.8%	9.8%
15	411,457	**41.9**	36.5	**38.7**	33.3	7.6%	8.8%

Table 10 Raft foundation's rotation due to the SSE Loads applied along the positive and negative y-axis directions.

Side	Load +y axis		Load -y axis	
	Rotation (Rad)	θ°	Rotation (Rad)	θ°
15,261-15,196	1.30×10^{-4}	7.45×10^{-3}	1.53×10^{-4}	8.79×10^{-3}
111,351-108,770	1.30×10^{-4}	7.45×10^{-3}	1.67×10^{-4}	9.55×10^{-3}
226,619-226,626	8.67×10^{-4}	4.97×10^{-3}	1.60×10^{-4}	9.17×10^{-3}
332,197-332,132	1.67×10^{-4}	9.55×10^{-3}	2.28×10^{-4}	1.31×10^{-2}
411,457-411,392	1.60×10^{-4}	9.17×10^{-3}	2.00×10^{-4}	1.15×10^{-2}

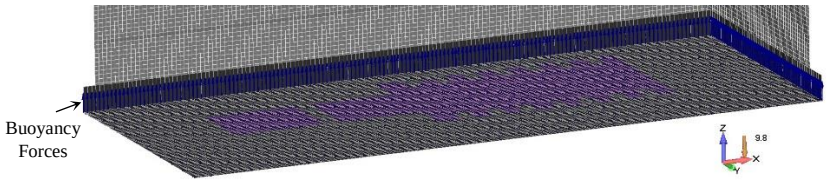

Figure 45 Model B (SSI). Buoyancy forces applied on the base of the raft foundation.

The final set of analyses that were performed herein assumed the application of the buoyancy forces at the base of the foundation (see Fig. 45) for the case where the water table was found to be at the surface of the soil (the entire underground structure is assumed to be submerged underwater). Therefore, the buoyancy forces were computed by using the total volume of the RB which is located underground ($V_{U.G.}$ = 58,024.625 m^3) and by multiplying by the corresponding nominal weight of water (γ_w = 10 kN / m^3). Based on these calculations, it was found that the maximum buoyancy force was approximately equal to 40% of the total RB weight. This is a first indication that the RB will not phase any uplift issues due to buoyancy forces, even in the case of a dynamic excitation that will force the water porous pressure to increase thus decrease the friction stresses along the retaining wall-soil interfaces. The volume of the entire building was calculated for the case where the whole structure is assumed to be underwater, whereas the derived buoyancy force was found to be smaller than the RB weight. This numerical finding is attributed to the heavy RC framing system of the building and the fluid found in the reactor's pool and the spent fuel storage that also significantly contribute to the overall weight. The total volume of the structure was computed to be equal to 84,165 m^3, where the corresponding total mass of the RB was calculated to be equal to 1,481,249.3 kN. Therefore, if the volume of the entire building is assumed to be underwater, the derived buoyancy force will not be able to make the structure float.

After applying the buoyancy forces on the base of the raft slab (see Fig. 45), the push over analysis was executed for both scenarios of SSE loads that foresaw the application of the horizontal forces along the

positive and negative y-axis directions. Fig. 46 shows the deformed shapes and displacement y-axis contours for the two load combinations as they resulted from the numerical analyses. As it can be seen, the deformed shapes and the maximum horizontal displacements are similar to those presented in Figs. 39 and 43, therefore, the buoyancy forces did not significantly affect the overall mechanical behavior of the structure. This can be also confirmed from the derived von Mises stress contours shown in Fig. 47, where it is easy to observe that the stress distribution and magnitudes were also similar to those resulted when the buoyancy forces were not accounted for. In Fig. 48, the numerically obtained von Mises stresses can be depicted for the soil domain that supports the raft foundation for the case where the buoyancy loads are accounted for.

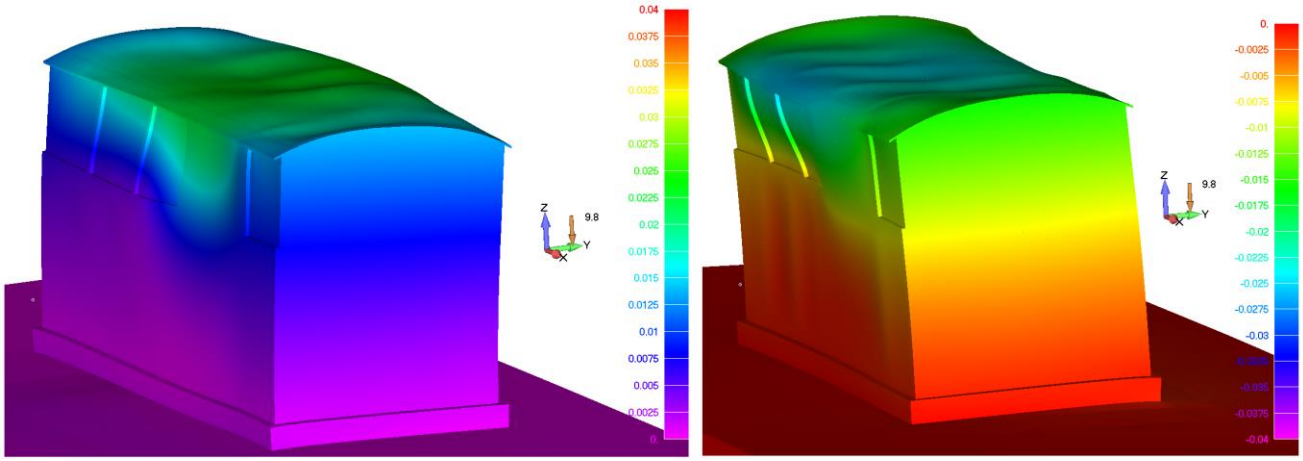

(a) (b)

Figure 46 Model B (SSI). Deformed shape and y-axis displacement contour due to the SSE loads along the (a) positive and (b) negative y-axis. Case with buoyancy forces.

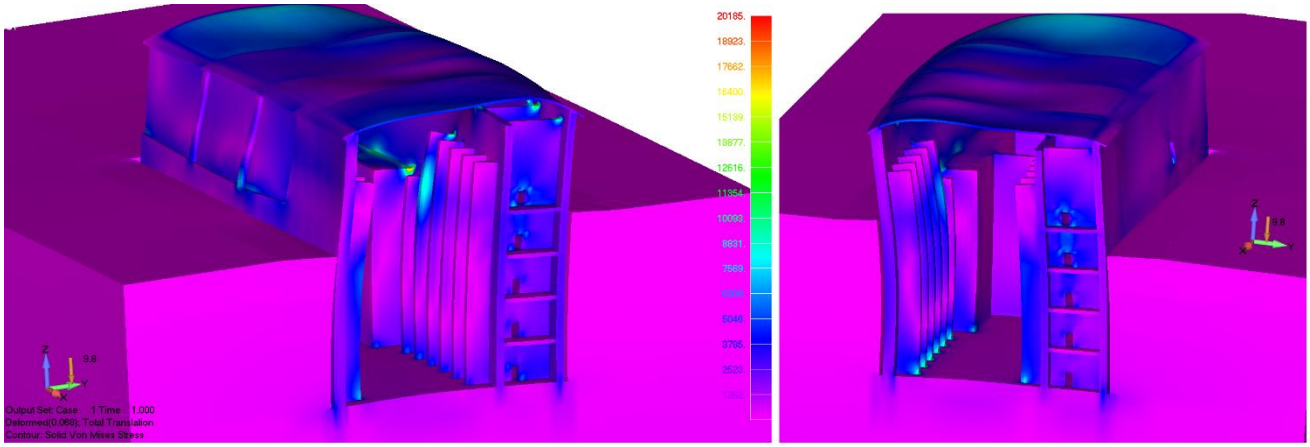

(a) (b)

Figure 47 Model B (SSI). Von Mises stress contour in kPa and deformed shapes due to the SSE loads along the (a) positive and (b) negative y-axis. Case with buoyancy forces.

Table 9 shows the new recorded settlements at the 15 monitored nodes located on the raft foundation. According to the numerical findings, the settlement was smaller in comparison to the previous analyses, but did not decrease in a proportional manner, as one would expect. In this case the buoyancy forces were approximately equal to half of the weight of the structure, therefore, the settlement should have exhibited a similar decrease, which does not comply with the obtained numerical results. This mechanical phenomenon is attributed to the vertical pressure of the soil that is applied directly on the raft foundation foot that extends 1 m beyond the retaining walls, providing a mechanism that behaves as an anchor thus resists to the buoyancy forces that attempt to uplift the structure. The decrease in terms of settlement was computed and also given in Table 9, comparing the analysis with and without buoyancy forces, where it was found that the nodes located

on the perimeter of the raft slab (i.e. 15,196/15,261/411,392/411,457), exhibited the lowest settlement decreases, while node 226,580 that is located at the center of the raft foundation was the node with the largest settlement decrease. This indicates that the raft foundation behaves as a slab that undertakes a uniform distributed load (along the positive z-axis) and it is supported at its four edges with rotational and vertical springs (due to the soil domain). Of course in this case the loads resulting from the reactor pool's fluid self-weight (gravitational direction -z) are simultaneously applied at the top side of the raft foundation, in addition to the self-weight loads from the steel sheet that is used to leakage proof the pool. Finally, the loads from the shear walls are also affecting the overall deformation of the 3 m thick raft foundation, which is found to provide a rigid base for the RB according to the numerical findings of this investigation. It must be noted here that the steel sheet that is used to leak proof the reactor pool, was assumed to have a thickness of 7 mm and it was accounted for as a dead load applied directly on the concrete surface of the model.

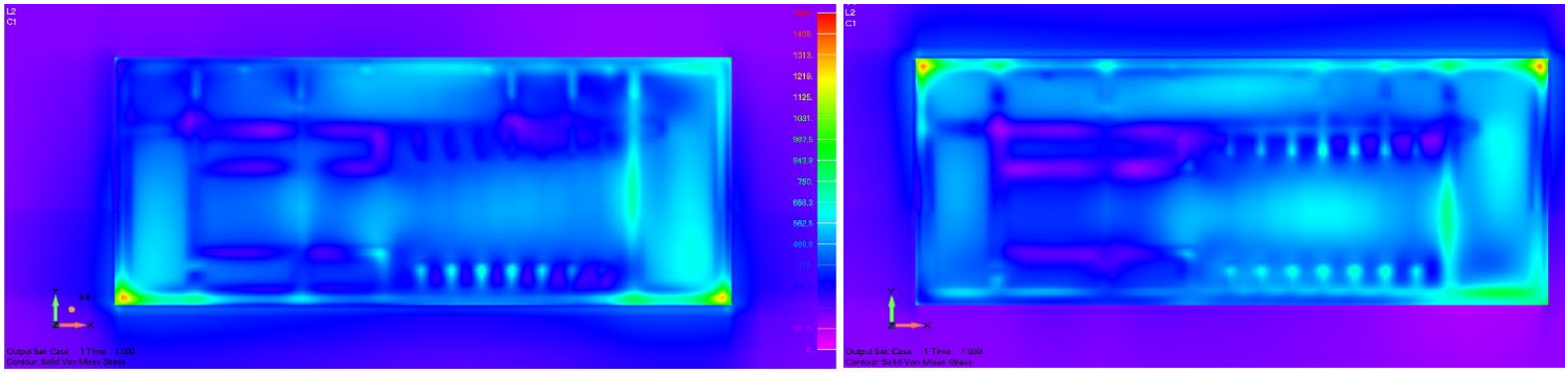

(a) (b)

Figure 48 Model B (SSI). Von Mises stress contour in kPa, developed on the foundation-soil interface due to the SSE loads along the (a) positive and (b) negative y-axis. Case with buoyancy forces.

Based on the modeling assumptions of this work, which had as a main objective the study of the mechanical behavior of the RB framing system under seismic loads with SSI considerations, the structure was studied through static push-over analysis by applying the maximum expected load along the corresponding global axis of the structure. It is evident that by performing a dynamic analysis by using different accelerograms it could result into more information related to the dynamic behavior of the structure but it would not guarantee the development of the maximum expected seismic load. Therefore, the developed models in this research work aimed in capturing the maximum expected stress and deformation magnitudes in both concrete and soil domains, where the maximum seismic loads are directly applied on the structure without accounting for any mechanisms that will potentially decrease the expected developed inertia forces. One of these mechanisms is energy dissipation due to the friction stresses that develop at the retaining walls-soil interface during the dynamic excitation. In addition to that, the fluid found inside the two pools will behave as a damper during a dynamic event that will lead to additional energy dissipation at an overall mechanical response level. Therefore, the actual expected mechanical behavior of the RB during a realistic dynamic excitation would foresee mechanisms that will consume energy leading to a smaller deformation and stress development.

It is also important to note at this point that, if a stiffer soil profile is selected (Ground Type A), the corresponding soil stiffness will increase considerably thus the expected stress concentrations within the concrete domain will be higher at the superstructure. This is partially true, given that according to the Eurocode 8 provisions the corresponding seismic loads will decrease by 17% due to the change of the soil type form B to A, where the parameter S will decrease from 1.2 to 1.0, hence causing the resulted seismic loads to decrease as well. Therefore, the realistic assumption of choosing a Ground Type B led to a loading scenario that derived significantly higher seismic loads and eventually higher stress magnitudes within the concrete and soil domains.

Finally, phenomena such as shrinkage (due to concrete bleeding, curing and heat) and creep were not accounted for through the analysis presented in this research work, which can affect the mechanical behavior of concrete through time. These material nonlinearities can be indirectly accounted for by modifying the material parameters of steel and concrete, whereas this was not within the scope of this work. In regards to other types of loads such as a tsunami strike, the direct solution to this natural hazard is to eliminate this loading type by choosing a RB site location that is found at an elevated terrain, thus the structure will not pose any tsunami exposure. If this is not an applicable solution given the selected location's terrain, then further investigation is deemed necessary in re-designing the framing system accordingly and reassuring that it will be able to withstand this type of extreme natural event.

4. Conclusions

Several new nuclear power plant designs are being proposed or are under investigation and development around the world. SMRs have many attractive features able to substantially improve safety and reliability of operations. While many proposals exist, CAREM-25, SMART and NuScale SMRs seem to be more industrially mature than other configurations. These plants were presented and discussed in section 2 of this manuscript. NuScale SMR was chosen, as a possible candidate to be implemented in Chile, due to its very advanced design, safety features and capacity to undergo shutdown without any external intervention incorporating all engineering post Fukushima-Daiichi safety enhanced considerations. For these reasons this was also the plant type that was chosen to be further structurally investigated herein.

The main objectives of this research work were to investigate the mechanical behavior of the NuScale SMR reactor building under different loading conditions by considering the SSI effect. The adopted geometry that was studied in section 3, foresaw an asymmetric design in an attempt to investigate a more geometrically non-canonic problem. Two software were used in order to study the mechanical behavior of the structure, SAP2000 and Reconan FEA. The validation of the 3D detailed model that was developed and analyzed with Reconan FEA, was performed through the use of SAP2000. Both software were also used to perform a modal analysis of the RB and study the carrying capacity of the RC beams placed at the arch shaped roofing system of the plant. After the numerical investigation was performed, the numerically obtained results from the modal and static analyses by using the two software showed that the differences in terms of computed modes and displacements were small. Additionally, the modal analysis of the structure revealed that the building exhibits relatively low fundamental periods given the fact that approximately 65% of the structure is underground, while the thick shear walls induce significant stiffness to the system.

An arch beam was isolated and studied independently in section 3.5 through the use of 3D detailed modeling and the simplest hinge model. Based on the vertical push over analyses performed, it was found that the detailed approach was able to capture significant nonlinearities related to the cracking of the beam thus derived a 12.5% smaller predicted capacity compared to the beam model that used plastic hinges. This numerical phenomenon is attributed to the stiffer behavior of the beam FE and the hinge model that fail to capture the exact mechanical behavior of the arch beam during the vertical push over analysis. Additionally, based on the numerical investigation it was found that the maximum capacity of the arch beam was sufficient to carry any load applied on the roofing system of the RB.

The first full-scale 3D detailed RB model was constructed by using the 8-noded hexahedral element that treats cracking through the smeared crack approach and the steel bars are modeled through the use of embedded rebar elements. This model was used to study the development of cracks due to the service loads that foresaw the application of the self-weight of the structure and the lateral soil pressures. Based on the nonlinear analysis it was found that the South retaining wall required to be redesigned (based on the initial assumed framing system), while the modified framing system was found to be able to maintain low stress and deformation magnitudes.

From the computational point of view, according to the FE analysis, the constructed 3D detailed model incorporated more than 2.7 million embedded rebar elements and 181,076 hexahedral elements. Even though the resulted large-scale model generated a significant computational demand, the numerical analysis was able to finish in a reasonable time. A parallel algorithm was developed and used here for generating the embedded rebar elements. The parallel embedded rebar mesh generation algorithm will be presented in a future publication.

Furthermore, the comparison between the two models that foresaw the discretization of the structure through shell/beam and hexahedral FEs, respectively, showed a good agreement in terms of deformation. For the case of the computed stresses, the SAP2000 model was found to have higher stresses at the joints, where the arch beams connected with the exterior shear walls. This was attributed to the modeling approach that foresaw the transfer of the high bending moments, shear and axial forces developed at the joints through a single node, which is a numerical deficiency that is alleviated when the more accurate hexahedral element is used to discretize the 3D domain of the structural framing system. In general, the computed stresses that derived from the two models were in a good agreement. Furthermore, it was noted that even though the hexahedral element provides with the ability of performing a more accurate analysis in comparison to the model that uses the shell FE, the computational increase is significantly higher when the solid element is engaged, therefore, the required computational time to solve the numerical problem is significantly longer. This is one of the main reasons why professional Civil Engineers still prefer the less accurate but computationally efficient modeling approach that foresees the use of shell and beam-column FEs.

A numerical investigation was performed so as to study the mechanical behavior of the RB under earthquake loads. The numerical results that were obtained through the use of the second Reconan model that foresaw the discretization of both concrete and soil domains with the hexahedral element (without embedded rebars), were discussed in section 3.8. Eurocode 8 was used so as to compute and distribute the seismic loads that derived from a 1.732g PSa. The seismic load calculations that adopted the fundamental period that was numerically computed, resulted the prementioned elastic spectrum acceleration of 1.732g, which was in line with the maximum PSa (1.73g) that occurred during the 2010 Chile earthquake (this PSa corresponded to structures with a fundamental period of 0.1 seconds [45]). Numerical analyses were performed herein that foresaw both scenarios related to the buoyancy forces (on and off), where for the case that buoyancy forces were accounted for, it was assumed that the entire underground facility was submerged in saturated soil. The seismic analyses revealed that the structure was able to undertake the applied earthquake loads without any problems, where the overall behavior was found to be relatively stiff due to the geometry of the structure and the underground facility that reached a depth of -25 m.

In terms of stress concentrations, the concrete domain was found to be able to maintain low stress levels without developing any major damages, where the raft foundation exhibited a mechanical behavior that was found to provide a sufficiently rigid support to the entire building. The soil medium was also found to be able to withstand the developed stresses without any failures due to high compression as a result of the superstructure loads. Nonetheless, it is important to state here that, the soil properties are always site-dependent and a different soil profile can result into a different SSI mechanical response. Overall, the NuScale SMR reactor building was found to be earthquake proof due to its shape and the large underground facility that provides the required support through which the superstructure loads can be safely transferred to the soil medium during an earthquake event. In addition to that, the 35% of the structural framing system that is found to be above the ground level does not allow for the development of large inertia forces (compared to a hypothetical scenario where the RB was designed to be above ground level), which is a common dynamic characteristic of short RC structures with shear walls that are not prone in developing extreme inertia forces due to resonance.

Modular nuclear power plants offer unprecedented economic benefit with respect to larger plants. They can be built with lower capital costs, reduced investment risks, reduced cost of capital and high flexibility in the needed number of cores. Mass production in factories, reduced construction schedule and rapid capacity of installation are all positive aspects that could benefit Chile for a rapid nuclear expansion that will further support the economic growth of the country by providing basic services such as electricity and water in off-grid areas. NuScale SMR offers simple and inherently safe design through an integral approach, reduced size, independent decay heat removal and passive safety features.

As future research objectives that immerse from the research work presented herein, the 3D SSI model will be integrated to include the Reactor Control and the Reactor Waste Buildings to further study the mechanical behavior of the soil medium under dynamic analysis. In addition to that, the 3D detailed model will be included within the SSI model in order to achieve maximum accuracy in terms of modeling the exact geometry and material behavior of both soil and concrete domains, where the level of developed damage will be investigated. This will require the use of a high performance CPU system and parallel processing algorithms in solving this mega-scale numerical problem. The study of the mechanical behavior of the structure under hydrodynamic loads due to a tsunami impact is also a very important extreme loading scenario that requires to be studied in order to assess the structure's vulnerability when dealing with this type of natural hazard, thus this will be also a subject of future investigation.

References

[1] Stevenson, J.D., Summary of the historical development of seismic design of nuclear power plants in Japan and in the US, Nuclear Engineering and Design, 2014, **269**:160-164.

[2] Anawat, S. et al., Lessons Learned from the 2011 Great East Japan Tsunami: performance of Tsunami countermeasures, coastal buildings, and Tsunami evacuation in Japan, Pure and applied geophysics, 2013, **170**:993-1018.

[3] Oka Y., Bittermann D. (2015), Implications and Lessons for Advanced Reactor Design and Operation. In: Ahn J., Carson C., Jensen M., Juraku K., Nagasaki S., Tanaka S. (eds) Reflections on the Fukushima Daiichi Nuclear Accident. Springer, Cham.

[4] Guarnieri F. (2017), The Fukushima Daiichi Nuclear Accident: Entering into Resilience Faced with an Extreme Situation. In: Ahn J., Guarnieri F., Furuta K. (eds) Resilience: A New Paradigm of Nuclear Safety. Springer, Cham.

[5] Alvarengaa, M.A.B. and Frutuoso E Melo, P.F., Including severe accidents in the design basis of nuclear power plants: An organizational factors perspective after the Fukushima accident, Annuals of Nuclear Energy, 2015, **79**:68-77.

[6] Park, J.W., Seol, W.-C., Considerations for severe accident management under extended station blackout conditions in nuclear power plants, Progress in Nuclear Energy, 2016, **88**:245-256.

[7] Saji, G., Safety goals for seismic and tsunami risks: Lessons learned from the Fukushima Daiichi disaster, Nuclear Engineering and Design, 2014, **280**:449-463.

[8] Furuta K., Kanno T. (2017), How the Fukushima Daiichi Accident Changed (or not) the Nuclear Safety Fundamentals? In: Ahn J., Guarnieri F., Furuta K.. (eds) Resilience: A New Paradigm of Nuclear Safety. Springer, Cham.

[9] Sutou, S., A message to Fukushima: nothing to fear but fear itself, Genes and Environment, 2016, **38:**12, https://doi-org.uai.idm.oclc.org/10.1186/s41021-016-0039-7.

[10] Saghafi, M. and Ghofrani, M. B., Accident management support tools in nuclear power plants: A post-Fukushima review, Progress in Nuclear Energy, 2016, **92**:1-14.

[11] Wu, W.-H., Liao, L.-Y., Emergency operating procedures improvement based on the lesson learned from the Fukushima Daiichi accident, Nuclear Engineering and Design, 2016, **309**.

[12] Wu, W.H., Liao, L.Y., Emergency operating procedures improvement based on the lesson learned from the Fukushima Daiichi accident, Nuclear Engineering and Technology, 2014, **46**(2):207-216.

[13] Song, J.H. and Kim, T.W., Severe Accident issues raised by the Fukushima accident and improvements suggested, Nuclear engineering and Technology, 2014, **46**:207-216.

[14] IAEA (International Atomic Energy Agency) Advances in Small Modular Reactor Technology Developments, 2014.

[15] Ashok Kumar Upadhyay, Karuna Jain, Modularity in nuclear power plants: a review, Journal of Engineering, Design and Technology, 2003, **14**(3):526-542.

[16] Ozturk, I., Measuring the impact of alternative and nuclear energy consumption, carbon dioxide and oil rents on specific growth factors in the panel of Latin American countries, Progress in Nuclear Energy, 2017, **100**:71–81.

[17] Gutierrez, Gonzalo, Antecedents and perspectives on the Development of nuclear Energy in Chile, ICPP2010 & LAWPP2010, Journal of Physics: Conference Series, 2014, **511** 012089.

[18] Ureta S., A very public mess: problematizing the "participative turn" in energy policy, Energy Research and Social Science, 2017, **29**:127-134.

[19] Marcel, C.P. et al., Stability of self-pressurized, natural circulation, low thermo-dynamic quality, nuclear reactors: The stability performance of the CAREM-25 reactor, Nuclear engineering and Design, 2013, **265**:232-243.

[20] Gimenez, M., Schlamp, M., Zanocco, P., Gonzalez, J., & Vertullo, A. (2002). CAREM-25 accident analysis (IAEA-CSP-14/P), International Atomic Energy Agency (IAEA).

[21] Kim, K.K. et al., SMART: The First Licensed Advanced Integral Reactor, Journal of Energy and Power Engineering, 2014, **8**:94-102.

[22] S.K. Zee, Design Report for SMART Reactor System Development, KAERI/TR-2846/2007, KAERI, Taejon, 2007.

[23] Ingersoll, D.T., Houghton, Z.J., Bromm, R. and Desportes, C., NuScale small modular reactor for co-Generation of Electricity and Water, Desalination, 2014, **340**:84-93.

[24] Ingersoll, D.T. et al., Integration of NUSCALE SMR with Desalination Technologies, Proceedings of the ASME 2015 Small Modular Reactors Symposium SMR2014, April 15-17 2014, Washington D.C., USA.

[25] Ahmed, S.A., Hani, H.A., Al Bazedi, G.A. et al., Small/medium nuclear reactors for potential desalination applications: Mini review, Korean J. Chem. Eng., 2014, **31**: 924-929.

[26] Reyes, J.N., Nuscale Plant Safety in response to Extreme Events, Nuclear Technology, 2012, **178**(2):153-163.

[27] Chávez-Rodríguez, M. et al., The role of LNG and unconventional gas in the future natural gas markets of Argentina and Chile, 2017, **45**:584-598.

[28] SAP2000, Integrated Software for Structural Analysis and Design, CSI Inc. https://www.csiamerica.com/products/sap2000

[29] Reconan FEA v1.00, Finite Element Analysis Software Manual, 2010.

[30] EN1992-1-1, Eurocode 2 (2004), Design of concrete structures.

[31] Markou, G. and Papadrakakis, M., Accurate and computationally efficient 3D finite element modeling of RC structures, Computers and Concrete, 2013, **12**(4):443-498.

[32] Markou G. and Papadrakakis M., An efficient generation method of embedded reinforcement in hexahedral elements for reinforced concrete simulations, Advances in Engineering Software ADES, 2012, **45**(1):175-187.

[33] Markou, G., Christos, M. and Papadrakakis, M., Cyclic Nonlinear Analysis of Large-Scale Finite Element Meshes Through the Use of Hybrid Modeling (HYMOD), International Journal of Mechanics, 2017, **11**(2017):218-225.

[34] Mourlas, Ch., Papadrakakis, M. and Markou, G., A computationally efficient model for the cyclic behavior of reinforced concrete structural members, Engineering Structures, 2017, **141**:97-125.

[35] Rashid, Y.M. (1968), Ultimate strength analysis of prestressed concrete vessels, Nucl Eng and Des, **7**:334-344.

[36] Gonzalez-Vidosa, F., Kotsovos, M.D. and Pavlovic, M.N., A three-dimensional nonlinear finite-element model for structural concrete. Part 1: main features and objectivity study; and Part 2: generality study, Proceedings of the Institution of Civil Engineers, Part 2, Research and Theory, 1991, **91**:517-544.

[37] Lykidis, G.Ch. and Spiliopoulos, K.V., 3D solid finite element analysis of cyclically loaded RC structures allowing embedded reinforcement slippage, Journal of Structural Engineering-ASCE, 2008, **134**(4):629-638.

[38] Menegotto, M., and Pinto, P. E. (1973), Method of analysis for cyclically loaded reinforced concrete plane frames including changes in geometry and non-elastic behavior of elements under combined normal force and bending, Proceedings, IABSE Symposium on Resistance and Ultimate Deformability of Structures Acted on by Well Defined Repeated Loads, Lisbon, Portugal, 15–22.

[39] Markou G., Sabouni R., Suleiman, F. and El-Chouli, R., Full-Scale Modeling of the Soil-Structure Interaction Problem Through the use of Hybrid Models (HYMOD), International Journal of Current Engineering and Technology, 2015, **5**(2):885-892.

[40] New Greek Seismic Code (NEAK), Athens, 2000.

[41] EN 1998-1: Design of structures for earthquake resistance – general rules, seismic actions and rules for buildings, September 2005.

[42] ACI318-14, Building Code Requirements for Structural Concrete and Commentary, ACI Committee 318, 2014.

[43] Markou, G. (2013), Numerical Investigation of a 3D Detailed Limit-State Simulation of a Full-Scale RC Bridge, SEECCM III, 3rd South-East European Conference on Computational Mechanics, Kos Island, Greece, 12–14 June 2013.

[44] Alicia, B., Antonio, P., Laura, L. and Joseluis, S. (2010), The Chilean Earthquake of 27 February 2010: an overview, Disaster Assessment Unit, ECLAC, United Nations Publications.

[45] Boroschek, R. and Contreras, V., Strong Ground Motion from the 2010 Mw 8.8 Maule Chile Earthquake and Attenuation Relations for Chilean Subduction Zone Interface Earthquakes, Proceedings of the International Symposium on Engineering Lessons Learned from the 2011 Great East Japan Earthquake, March 1-4, 2012, Tokyo, Japan.

[46] Sextos, A.G., Manolis, G.D., Athanasiou, A. and Ioannidis, N. (2017), Seismically induced uplift effects on nuclear power plants. Part 1: Containment building rocking spectra, Nuclear Engineering and Design, 2017, **318**:276-287

[47] Bathe, K.J., Solution Methods for Large Generalized Eigenvalue Problems in Structural Engineering, Report UCSESM 71-20, Department of Civil Engineering, University of California, Berkeley, 1971.

[48] Markou, G., Mourlas, Ch., Bark, H. and Papadrakakis, M. (2018), Simplified HYMOD Non-Linear Simulations of a Full-Scale Multistory Retrofitted RC Structure that Undergoes Multiple Cyclic Excitations – An infill RC Wall Retrofitting Study, Engineering Structures, 176 (2018), pp. 892–916.